Bridging the Gap: Synthetic Radio Observations of Numerical Simulations of Extragalactic Jets

by

Nicholas Roy MacDonald

A Thesis Submitted to Saint Mary's University, Halifax, Nova Scotia in Partial Fulfillment of the Requirements for the Degree of

MASTERS OF SCIENCE

in

Astronomy

(Department of Astronomy and Physics)

August 15, 2008,Halifax, Nova Scotia

© Nicholas Roy MacDonald, 2008

Approved:

Dr. David Clarke
Supervisor

Approved:

Dr. Roby Austin
Examiner

Approved:

Dr. Luigi Gallo
Examiner

In presenting this thesis in partial fulfilment of the requirements for an advanced degree at Saint Mary's University, I agree that the Library shall make it freely available for reference and study. I further agree that permission for extensive copying of this thesis for scholarly purposes may be granted by the head of my department or by his or her representatives. It is understood that copying or publication of this thesis for financial gain shall not be allowed without my written permission.

(Signature) _____

Department of Astronomy and Physics

Saint Mary's University
    Halifax, Canada

Date _____

Contents

List of Figures

List of Tables

Acknowledgements

This work would not have been possible without the support and encouragement of my supervisor Dr. David Clarke, my friend and colleague Jon Ramsey and my fiancee Elizabeth Baxter. Together these three people formed a triumvirate, whose guidance and collective wisdom have allowed me to succeed these last two years. To them I dedicate this thesis.

Abstract

Bridging the Gap: Synthetic Radio Observations of Numerical

Simulations of Extragalactic Jets

by Nicholas Roy MacDonald

The standard paradigm for radio galaxies is based on high-speed plasma jets, formed in active galactic nuclei, which then penetrate into the surrounding intergalactic medium creating giant lobes of luminous material. These lobes then emit radio waves due to synchrotron radiation from high-energy electrons immersed in weak magnetic fields. Modern computational resources have allowed increasingly sophisticated magnetohydrodynamical (MHD) simulations of these plasma flows; however, simulating the emission from these jet models, and thus bridging the gap between theory and observation, remains a difficult task. I will present a semi-empirical model of synchrotron emission that I have incorporated into full three-dimensional MHD jet simulations. From these models I generate synthetic radio images that can be compared to actual observations. This thesis will present the results of this radio imaging procedure. By synthetically observing a source whose detailed structure is known beforehand, one can hope to gain insights into what real observations are telling us about these types of jets.

August 15, 2008

Chapter 1

Introduction

1.1 Radio Galaxies

1.1.1 Basic Morphology

Extragalactic Radio Sources (ERS) form a unique class of galaxies which radiate primarily in the radio passband. These include objects ranging in size from the very compact steep spectrum sources with scale lengths $\sim$ kpc to extended radio sources that can measure up to $\sim$ Mpc in length (Bagchi et al. 2007). This work is concerned primarily with the latter group which make up a small minority of all ERS. The majority of the radio emissions from these extended ERS originate not from within the *core* of the galaxy itself but from extended *lobes* which are located in nearly symmetric positions at large distances ($\sim 10^2$ kpc) from the central active galactic nucleus (AGN) as shown in Fig. 1.1. Regions of intense radio emission, referred to as *hot spots*, are sometimes contained within these lobes. Enormous collimated *jets* of plasma are observed to emanate from the AGN and extend to the distant lobes. These jets, along with the lobes, emit nonthermal radio emission known as synchrotron radiation.

Over six hundred extended ERS have been discovered and are classified into two categories, FRI and FRII (Fanaroff & Riley 1974), based on their observed radio
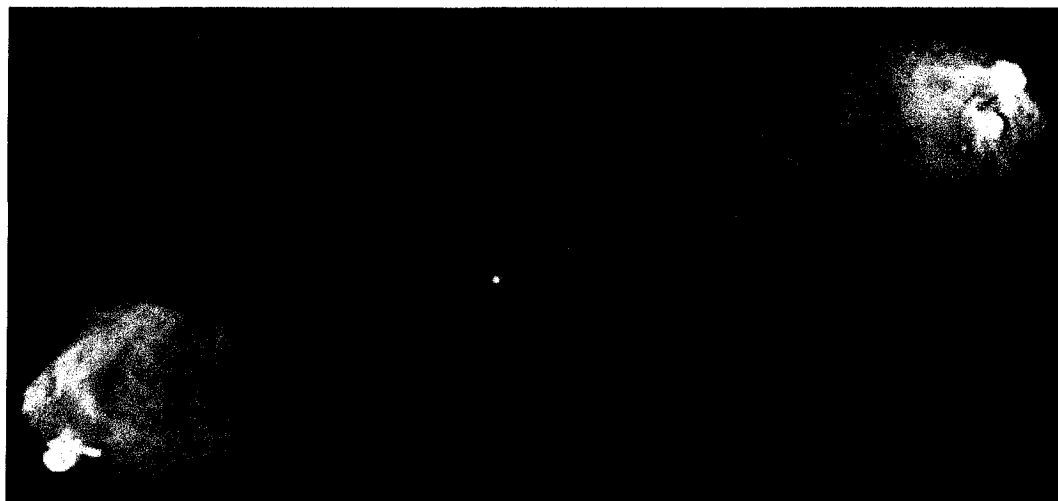
Figure 1.1: Radio image of Cygnus A at 6 cm (Image courtesy of NRAO/AUI).

morphologies and radio powers at 178 MHz (FRI : $P_{128} < 2 \times 10^{32}$ ergs str^{-1}, FRII : $P_{128} > 2 \times 10^{32}$ ergs str^{-1}). Examples of both morphologies are shown in Fig. 1.2. FRI-type galaxies exhibit jet-dominated emission and are typically found in rich cluster environments. FRII-type galaxies exhibit lobe-dominated emission and are typically found in isolated regions outside of galaxy clusters. These differences in environment are believed to be the cause of the two different morphologies. The intracluster medium in the rich cluster environment destabilizes FRI jets, while the isolated environment of FRII type galaxies allows their jets to remain intact up until impact with the surrounding intergalactic medium (IGM) creating the hot spots unique to this class.

1.1.2 The Standard Model

High-energy plasma is assumed to be embedded in a dense, lower temperature fluid that dominates the dynamics of the flow. As shown in Fig. 1.1 there are four main
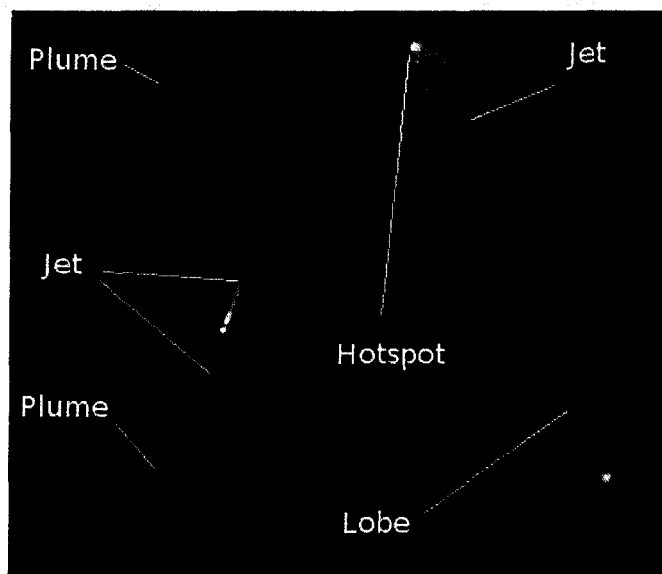
Figure 1.2:   Radio morphologies of FRI (left) and FRII (right) type galaxies (Image courtesy of NRAO/AUI). The core is the central point from which the jets emanate.

components of radio galaxies: the *core*, the *jets*, the *hot spots* and the *lobes*. High-energy electrons are initially produced in the central AGN, which is usually observed as a compact, partially self-absorbed core (PSO). This central core corresponds to the 'engine' driving these flows and is the ultimate source of energy that powers the radio lobes. The core generates a huge amount of energy ($\gg 10^{45}$ ergs s^{-1}) in a relatively small region ($\ll pc$; Carilli & Barthel 1996). On scales of $\sim$ kpc, jets are often seen emanating from one or both sides of the AGN. These jets are produced and collimated in the innermost regions of the AGN by a physical mechanism that derives its energy from accretion onto a black hole (Baschek 2001).

The seminal paper on magnetized disks and jets was published by Blandford and Payne (1982). They derived self-similar steady state solutions of the ideal magnetohydrodynamic (MHD) equations of a cold, axially symmetric magnetospheric flow from
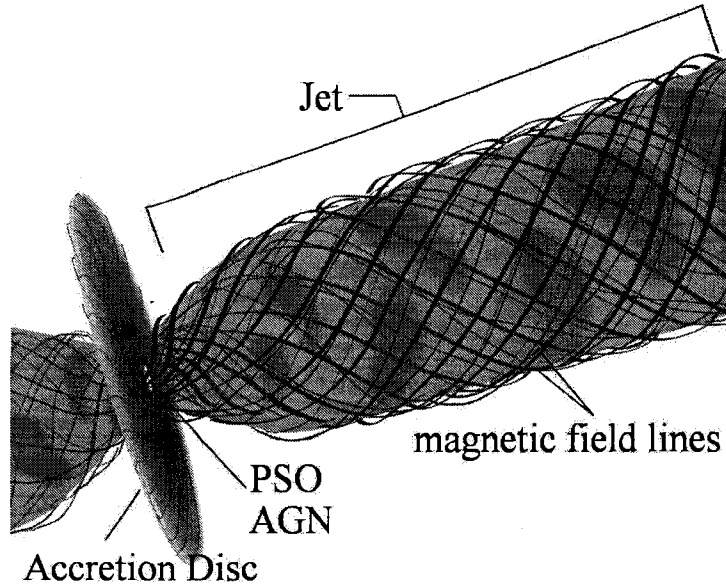
Figure 1.3: Artist's rendition of the Blandford & Payne mechanism [Image courtesy of NASA/ESA and Ann Feild (STScI)].

a Keplerian disc. They assumed that open poloidal magnetic field lines co-rotating with the flow at the Keplerian velocity thread the accretion disk. These magnetic field lines are then 'coiled-up' (Fig. 1.3) as the disk rotates, forming a magnetic *helical* structure along which matter is centrifugally driven.

The rotation of the accretion disc results in the generation of a toroidal magnetic field that becomes dominant at large distances from the AGN close to the rotation axis. Provided the poloidal component of the magnetic field lines makes an angle of less than 60° with respect to the disc surface, the magneto-centrifugal force overcomes the gravitational force acting inwards and matter is then centrifugally driven along the field lines. The toroidal field consequently collimates the flow into a jet.

These jets, particularly in the FRII class, propagate unhindered until they terminate in a strong shock on impact with the IGM. Most basic dynamic models of ERS

predict the formation of two distinct shocks in the jet terminal region: the *Mach disk* and the *bow shock*. The *Mach disk* effectively halts the incoming jet. The weaker *bow shock* accelerates and heats the surrounding ambient medium into which the jet propagates. The two fluids (shocked jet material and shocked ambient medium) meet in pressure balance along a contact discontinuity. The high pressure shocked jet material then expands out of the hot spots inflating the synchrotron emitting radio lobes.

Jet morphologies typically exhibit *wiggles* along the initial length of the jet. This has led to theories of jet precession in which an initially tilted accretion disk in the central engine can become unstable resulting in the observed opening morphologies (Dal Pino 2005).

Multiple hot spots are often observed in the lobes of ERS. Kelvin-Helmholtz instabilities occurring along the length of the jet cause the flow to alter direction on time-scales shorter than the time it would take for an abandoned/secondary hot spot to fade to the background intensity level ($\sim 10^5$ yr) because of expansion and synchrotron losses (Carilli et al. 1988). The primary hot spot represents the current location where the jet impacts on the contact discontinuity separating the shocked jet and ambient medium (Carilli & Barthel 1996).

The 'wispy' filamentary structure observed in radio images of the lobes (Fig. 1.1) is consistent with 3-D MHD calculations which show a natural development of passive magnetic fields into 'bundles' of field structure (Clarke et al. 1993). These bundles of magnetic field result in filamentary synchrotron emission.

1.1.3 Physical Parameters

The main difficulty astronomers face when trying to deduce the physical conditions present in extragalactic radio sources is the absence of features in the spectra of these objects. Because of this lack of spectral information, even fifty-five years after the discovery of Cygnus A (Jennison & Das Gupta 1953), observers and theorists are still debating very basic questions concerning the physical conditions present in radio galaxies (Massaglia 2003).

Models of extragalactic jets depend on several parameters: the Lorentz factor (Γ), the Mach number (M), the jet-to-ambient density ratio (η) and the plasma beta (β). Unfortunately, none of the above parameters have been constrained directly by observations (Massaglia 2003).

There are two possible compositions of extragalactic jets: proton-electron pairs in which the electrons are relativistic and electron-positron pairs in which both particles are relativistic. Jet simulations of both compositions have shown identical jet dynamics and morphologies (Scheck et al. 2002). Therefore, jet composition remains an open question.

The jet-to-ambient density ratio (η) has only been constrained by a qualitative comparison between numerical simulations and observations. Simulations of supersonic, *underdense* jets resemble the morphologies observed in these radio galaxies. η could be as small as 10^{-5} in some sources (Massaglia 2003).

How does one estimate the magnetic field strength in an ERS? Most studies adopt the 'minimum energy' argument, first presented by Burbidge (1956), which relies on

	core	jet diameter	hot spot	lobe
size (kpc)	$\leq 10^{-3}$	$2 - 10^3$	5	$50 - 10^3$
B (T)		$\leq 10^{-7}$	10^{-7}	10^{-9}
$n_{e,\mathrm{rel}}$ (m^{-3})		$10^4 - 10$	$\leq 10^4$	$\leq 10^2$
α (spectral index)	0.0	0.6	0.6	0.9
v_{jet}/c	$\rightarrow 1$	10^{-1}	10^{-3}	10^{-3}

Table 1.1: Radio Galaxy Properties (Massaglia 2003)

the basic assumption that there is an equipartition between the relativistic particle energy density and the magnetic field. This assumption yields an empirical measure of the magnetic field which is dependent solely on measurements of synchrotron intensity (Tregillis et al. 2004). In addition, multi-frequency polarimetric imaging (Carilli & Barthel 1996) is used to determine the fraction of the total intensity which is linearly polarized. When corrections are made for Faraday rotation these polarization images can be used to determine the projected magnetic field structure in ERS. Polarization images of Cygnus A indicate that there are high ($\sim 70\%$) levels of fractional polarization in the radio lobes. These images show that the projected fields are parallel to the axis of the radio lobes. If the reason for this is that the fluid has "combed" the field lines parallel to the flow, this would imply that the lobes are not magnetically dominated. It is generally accepted that trace magnetic fields exist in ERS, and that hydrodynamic models should be sufficient in describing the dynamics of most jets; however, the magnetic fields are central to the synchrotron mechanism which results in the observed radio emission (Longair 1994).

Table 1.1 summarizes some of the best guesses at the various physical parameters in ERS.
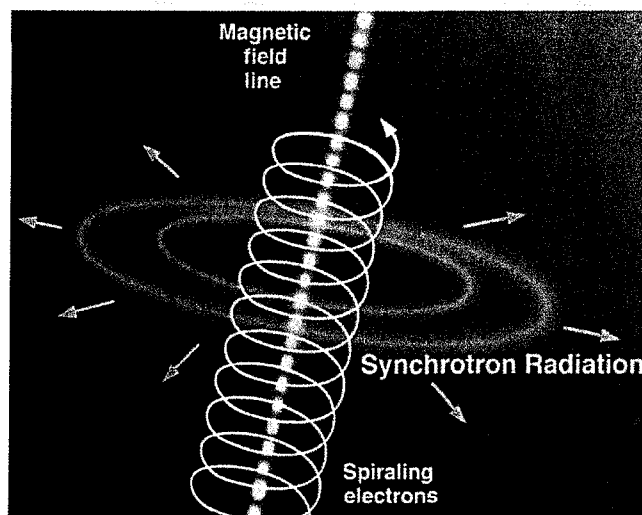
Figure 1.4: The synchrotron mechanism (Image courtesy of Gemini Observatory).

1.2 Synchrotron Radiation

Synchrotron radiation is a form of emission that dominates high energy astrophysics. It is primarily emitted by high-energy electrons accelerating along magnetic field lines (Fig. 1.4).

This continuum emission is *non-thermal* in nature and cannot be accounted for by thermal bremsstrahlung or blackbody radiation. A typical radio-source spectrum dominated by synchrotron radiation shows a steady featureless decline in intensity over many decades of frequency. Most synchrotron spectra obey the following power-law:

$$i(\nu) \propto \nu^{-\alpha} \, , \qquad (1.1)$$

where α is referred to as the spectral index and $i(\nu)$ is the synchrotron emissivity. To derive equation (1.1), one can follow Longair's derivation (1994): the rate of energy

loss due to synchrotron radiation[1] from a relativistic electron immersed in a magnetic field B is (mks units):

$$\frac{dE}{dt} = -\frac{2}{3}\frac{\sigma_t}{\mu_0 m_e^2 c^3} B^2 E^2 = -1.5782 \times 10^{12} B^2 E^2 , \tag{1.2}$$

where σ_t is the Thomson cross section for the electron (6.6524×10^{-29} m^2), μ_0 is the permeability of free space ($4\pi \times 10^{-7}$ kg m C^{-2}), m_e is the mass of the electron (9.1094×10^{-31} kg) and c is the speed of light (2.9979×10^8 m s^{-1}). The frequency about which the synchrotron emission is 'peaked' is referred to as the Larmor frequency and is given by:

$$\nu \sim \nu_l = \frac{\Gamma^2 e B}{2\pi m_e} , \tag{1.3}$$

where e is the charge of the electron ($e = 1.6022 \times 10^{-19}$ C), and Γ is the Lorentz factor of the electron [$\Gamma \equiv 1/\sqrt{(1 - v^2/c^2)}$]. Equation (1.3), when solved for Γ and substituted into the following expression for energy, in the relativistic limit, yields:

$$E = \Gamma m_e c^2 = m_e c^2 \left(\frac{2\pi m_e}{e}\frac{\nu}{B}\right)^{1/2} = 4.8935 \times 10^{-19} \left(\frac{\nu}{B}\right)^{1/2} . \tag{1.4}$$

In a constant magnetic field, differentiating equation (1.4) yields:

$$dE = 2.4468 \times 10^{-19} \nu^{-1/2} B^{-1/2} d\nu . \tag{1.5}$$

Consider now an ensemble of electrons emitting synchrotron radiation. Given a par-

---

[1]commonly referred to as synchrotron losses or synchrotron cooling

ticle distribution function for the electron population [$N(E)$ dE = the number of electrons per unit volume with energy between E and $E +$ dE], the net emissivity [$i(\nu)$ dν = power per unit volume of emitting fluid radiated at frequencies between ν and $\nu +$ dν] is given by:

$$i(\nu)\ \mathrm{d}\nu = -\frac{\mathrm{d}E}{\mathrm{d}t}\ \mathrm{N(E)}\ \mathrm{d}E\ . \tag{1.6}$$

There is ample observational evidence that the particle distribution function $N(E)$ is well approximated by the following power-law (Longair 1994):

$$N(E) = \kappa E^{-x}\ , \tag{1.7}$$

where κ is a proportionality constant and x is a power-law index. Substituting equations (1.2), (1.4), (1.5) and (1.7) into equation (1.6) yields:

$$i(\nu) \sim \kappa\ \nu^{(1-x)/2}\ B^{(1+x)/2}\ . \tag{1.8}$$

It follows that the frequency dependence of the emissivity is a power-law in agreement with equation (1.1), where the spectral index (α) is related to the power-law index (x):

$$\alpha = \frac{x - 1}{2}\ . \tag{1.9}$$

A further level of complexity arises since the synchrotron spectrum of an ensemble of electrons evolves with time. As shown in equation (1.2), synchrotron losses are proportional to B^2. Therefore, unless the electrons are being continuously re-

energized, the particle distribution function $N(E)$ will eventually be depleted. There are three analytic models that are widely used in fitting the temporal evolution of the synchrotron spectrum (Sohn et al. 2003): the continuous injection model (CI; Pacholczyk 1970), the Kardashev-Pacholczyk model (KP; Kardashev 1962; Pacholczyk 1970) and the Jaffe-Perola model (JP; Jaffe & Perola 1973). The CI model assumes a mixture of electron populations of various synchrotron ages with a continuous replenishment of fresh electrons. This analytic model is most applicable in the regions of strong shocks such as the hot spots. The KP model, in contrast, models a single injection of a power-law distribution of electrons subject to synchrotron losses, and furthermore assumes that the pitch angles[2] of the electrons remain constant as a function of time. This model is most applicable in regions such as the lobes where synchrotron cooling is dominant. Like the KP model, the JP model assumes a single injection of electrons, but also incorporates pitch angle isotropization. An illustration of the synchrotron spectra produced by these three models is shown in Fig. 1.5.

When the time evolution of $N(E)$ is accounted for, the emissivity as a function of synchrotron age (t_{syn}) may be written as:

$$i(\nu, t_{\mathrm{syn}}) = \begin{cases} \kappa_{\mathrm{new}} \ (B \ \sin\psi)^{(x+1)/2} \ \nu^{-(x-1)/2} & \nu < \nu_{br} \\ \kappa_{\mathrm{old}} \ (B \ \sin\psi)^{-2} \ \nu^{-(2x+1)/3} \ t_{\mathrm{syn}}^{-(x+5)/3} & \nu > \nu_{br} \ , \end{cases} \tag{1.10}$$

where ν_{br} is a critical 'break' frequency at which the two power-laws join, κ_{new} and κ_{old} are proportionality constants related to the total number density of relativistic electrons contained within each portion of the spectrum, and ψ is the angle between

---

[2]defined as the angle between the electron's velocity and the magnetic field
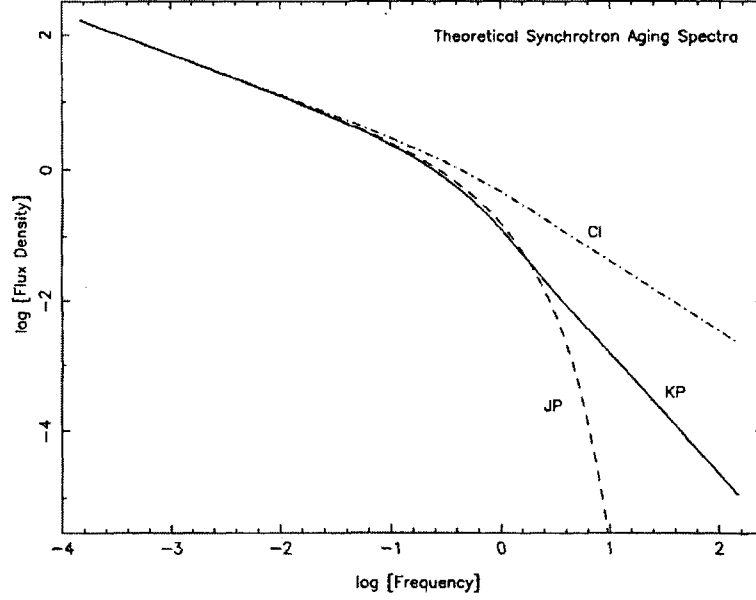
Figure 1.5: Examples of the three analytic models: CI, KP and JP (courtesy Carilli et al. 1991).

the magnetic field and the line-of-sight (Kardashev 1962). Synchrotron age (t_{syn}) is defined as the time since *injection* of the high-energy electron population, namely the time since the synchrotron spectrum was a single power-law out to infinite frequency (Carilli et al. 1991). Therefore, an 'aged' synchrotron spectrum is governed by two spectral indices. The first spectral index, α_{new}, is given by equation (1.9), and the second spectral index, α_{old}, is given by:

$$\alpha_{old} = \frac{2x + 1}{3} . \qquad (1.11)$$

For frequencies below ν_{br} the electrons are still energetic and emit a *young* (*flatter*) spectrum. At frequencies above ν_{br} the electrons have been depleted in energy because of synchrotron losses and emit an *aged* (*steeper*) spectrum.

An analytic expression for the synchrotron age of an ensemble of electrons can be obtained by dividing the expression for E [see equation (1.4)] by the expression for dE/dt [see equation (1.2)] and integrating (mks units):

$$t_{\text{syn}} = 6.4742 \times 10^5 \ \nu_{\text{br}}^{-1/2} \ B^{-3/2} \ . \tag{1.12}$$

Equation (1.12) can then be inverted to give the following expression for the break frequency:

$$\nu_{\text{br}} = 4.1916 \times 10^{11} B^{-3} \ t_{\text{syn}}^{-2} \ . \tag{1.13}$$

Equation (1.13) shows that as time progresses and the electrons age, the *break* in the spectrum moves toward lower frequencies. Thus, synchrotron radiation preferentially depletes energy at higher frequencies. An illustration depicting how synchrotron losses modify the spectrum over time is shown in Fig. 1.6.

For most known radio sources, α is observed to be within the range $0.75 < \alpha < 2.0$, corresponding to $x \sim 2.5$; however, Young et al. (2005) carried out a low-frequency analysis of a sample of ERS and found that the inner regions of these sources appear to have a fairly narrow spectral distribution around $\alpha \sim 0.55 \rightarrow x \sim 2.1$. These spectral index values reflect the initial acceleration of relativistic electrons along the jet as they emerge from the nucleus of the AGN. At high frequencies the spectra of ERS are observed to steepen (α increases) from this value. This spectral evolution has been explained as an effect of radiative aging of the electron populations. This would mean that regions of an ERS with $\alpha \sim 2.0$ are 'older' than those with $\alpha \sim 0.5$
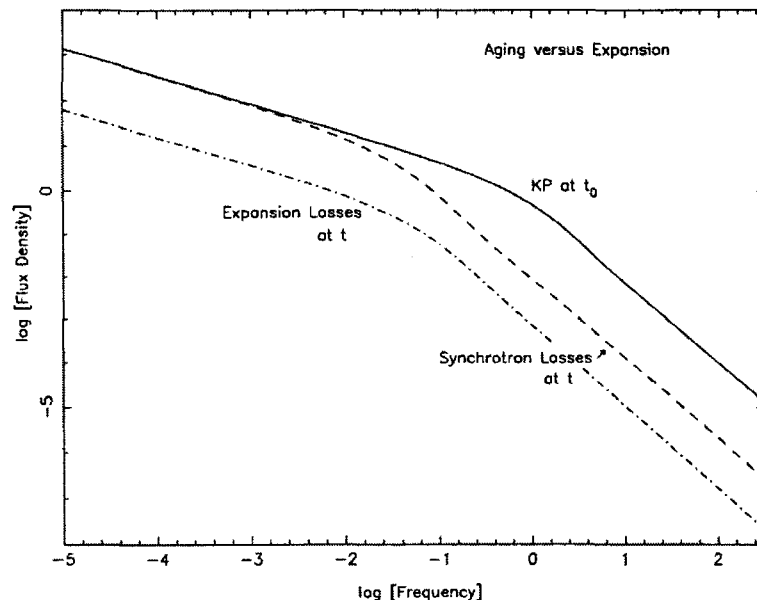
Figure 1.6: An idealized synchrotron spectrum illustrating the effects of synchrotron losses and adiabatic expansion (courtesy Carilli et al. 1991).

(Carilli et al. 1991). From an observational standpoint, spectral index variations in ERS can be used as a probe into the radiative gain and loss mechanisms affecting the populations of high-energy electrons (Treichel et al. 2001).

There is a discrepancy between the relatively young synchrotron ages ($\sim 10^6$ yr; Clarke et al. 1992) observed in the hot spots of ERS and the independent dynamical estimates of the source ages (Miley 1980). A source age, in contrast to synchrotron age, is the time in which sustained accretion in the central AGN, resulting in jet production, is active. Current models of accretion mechanisms in AGN suggest that the source ages of ERS are $\sim 10^8 - 10^9$ yr (Koide et al. 2000). These values are in agreement with simple observational constraints on source ages obtained from dividing the projected physical size of a radio galaxy by the estimated speed at which it has expanded to that size (Blundell & Rawlings 2000). This discrepancy between

synchrotron age and source age can be accounted for if some form of diffusive shock acceleration is occurring in the hot spots. Diffusive shock acceleration is a physical mechanism by which the high-energy electron populations can be *re-energized* through inelastic collisions with media on opposite sides of a shock front which have average velocities towards the shock boundary. The net effect of diffusive shock acceleration on the synchrotron spectrum is to shift the spectral break back to higher frequencies thus negating the effects of synchrotron losses.

After the plasma passes through the shock regions of the hot spots, it expands (adiabatically) back into the giant radio lobes that encompass the jet (Scheuer & Williams 1968). This expansion decreases the electron energy and magnetic field strength, further shifting the spectral break to lower frequencies and reducing the overall emitted flux as depicted in Fig. 1.6.

1.3   Observational Analysis

How does one set about disentangling all the various physical processes that contribute to the observed synchrotron spectra of a radio galaxy? Multi-frequency observations provide one approach. The relationship between spectral shape and radiative age allows one to study the growth and evolution of ERS by carefully measuring the synchrotron spectra throughout the source. A crucial ingredient in this study is the magnetic field intensity. Equation (1.12) shows that the synchrotron age depends more strongly on the magnetic field than the break frequency ($B^{-3/2}$ vs. $\nu_{br}^{-1/2}$). Unfortunately, no observational technique exists to determine *directly* the magnetic field
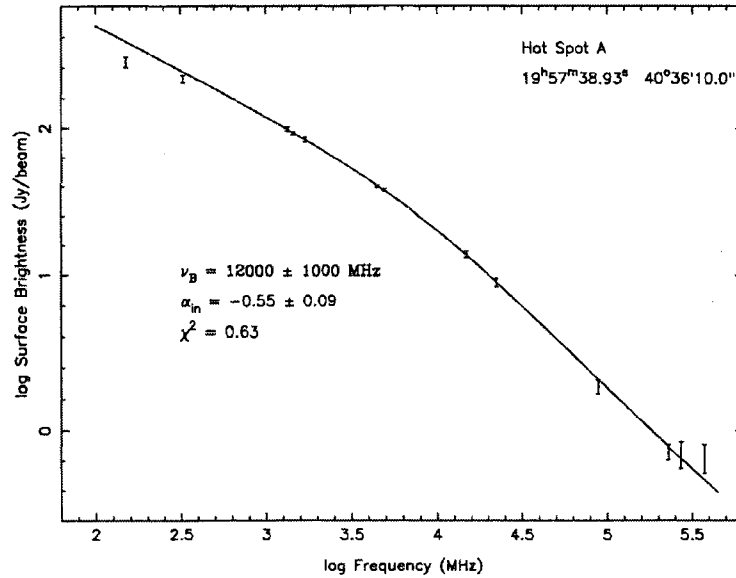
Figure 1.7: Spectral data for the primary hot spot in the western lobe of Cygnus A (4.5″ resolution). The solid line is the best fit CI spectral model. The parameters for the fit are listed on the plot. (courtesy Carilli et al. 1991).

strengths in ERS. Most standard studies *assume* constant minimum energy magnetic fields; however, complications in these analyses arise if, as is likely the case, the magnetic field varies with position and time $[B(\vec{r}, t)]$.

Carilli et al. (1991) carried out extensive multi-frequency (1.5×10^8 Hz $\rightarrow$ 2.2 $\times$ 10^{10} Hz) observations of Cygnus A in order to study the effects of spectral steepening at high frequencies. The observed spectra of the various regions (lobes, hot spots *etc.*) were fit with the various spectral models (KP, JP and CI). It was found that no one spectral model could account for all the spectral variations present in Cygnus A but rather the CI model best fit the hot spot spectra while the KP model best fit the lobe spectra. From this spectral modeling the best fit spectral parameters, namely, ν_{br} and α, were determined. An example of this spectral fitting is shown in Fig. 1.7.

Young spectral indices of $\alpha \sim 0.75$ were observed in the hot spot regions indicating

an underlying power-law index of $x \sim 2.5$ in agreement with standard theory. The resulting break frequency distribution for the lobes and hot spots of Cygnus A was plotted, showing a clear trend of decreasing break frequency with increasing distance from the hot spots ($\nu_{br} \sim 50$ GHz in the hot spots to $\nu_{br} \sim 750$ MHz in the lobes). Assuming a constant magnetic field of $B \sim 5 \times 10^{-9}$ T, the break frequencies were used to compute [see equation (1.12)] synchrotron ages for each position in Cygnus A. As expected, the age distribution showed a clear trend of increasing synchrotron age with increasing distance from the hot spots. The dominant energy loss mechanism in the lobes was found to be synchrotron radiation and not adiabatic expansion. The results of this observational analysis confirm the basic model presented in §1.1.2 in which high-energy electrons are accelerated through shocks in the hot spots and then expand back into the radio emitting lobes subsequently losing energy through synchrotron radiation. However, if magnetic field variations are present in Cygnus A, the age distributions determined by this analysis are no longer direct measures of the 'true' synchrotron ages.

Rudnick & Katz-Stone (1996) have developed a series of innovative, yet controversial, observational techniques that use multi-frequency data to elicit information about the underlying physics in radio galaxies without relying on the above assumption of constant magnetic fields. These techniques include: spectral tomography, colour-colour diagrams, and physical pair images, each described below in separate subsections. These techniques have been applied to a wide range of observations of ERS: Katz-Stone & Rudnick (1997), Katz-Stone et al. (1999), Blundell & Rawlings (2000), Treichel et al. (2001), Gizani & Leahy (2003) and Sohn et al. (2003).

1.3.1 Spectral Tomography

Spectral tomography describes a sequence of intensity images created through linear combinations of two input images at different wavelengths. For example, a spectral tomography gallery between 6 cm and 20 cm observations is created by constructing individual intensity images:

$$I_t = I_{20} - \left(\frac{\lambda_{20}}{\lambda_6}\right)^{\alpha_t} I_6 \, , \qquad (1.14)$$

where α_t is a "dial" that is "tuned" for each individual image over some useful range of spectral indices ($0.75 < \alpha_t < 2.0$). Spectral features *drop out* (relative to the local background) of a tomography image when α_t is equal to that feature's spectral index. This allows one to discern (by varying α_t) separate spectral components that would otherwise be blended together in a total intensity or two-point spectral index image. An example gallery for Cygnus A is shown in Fig. 1.8. This tomography sequence clearly isolates the different spectral components contained within Cygnus A West, namely, the hot spots, the jet and the lobe. The hot spots disappear first, indicating they have a flatter (younger) spectrum than the jet which does not drop out until frame nine.

1.3.2 Colour-Colour Diagrams

Colour-colour diagrams have numerous astrophysical applications. In radio astronomy they are used to examine the shape of a synchrotron spectrum. A two-point spectral index can be defined between any two intensity measurements, for example,
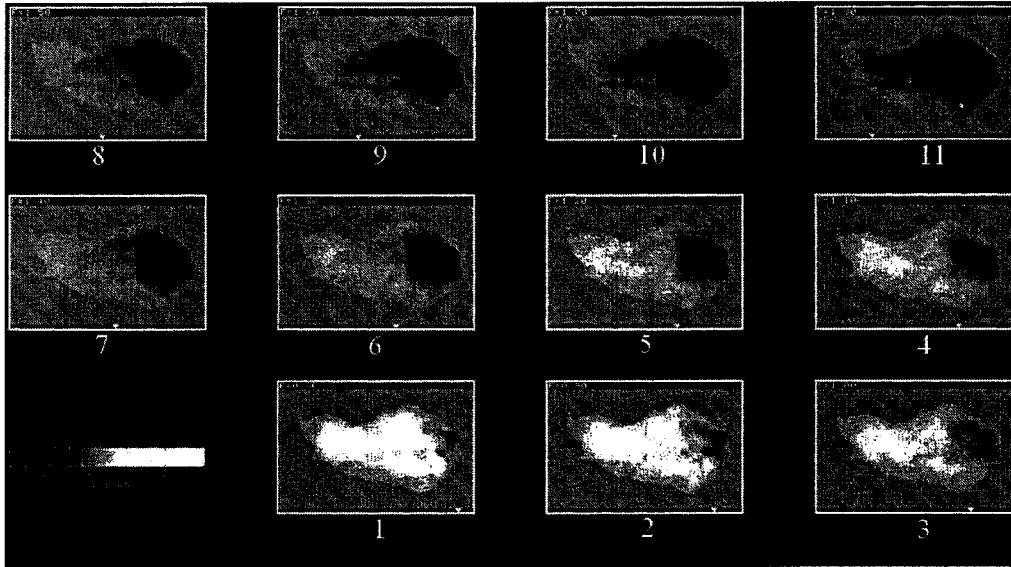
Figure 1.8: Spectral tomography gallery for Cygnus A West. The tomography sequence runs from $0.8 < \alpha_t < 1.8$ with a step size of 0.1 (courtesy Katz-Stone & Rudnick 1996).

I_2 and I_6 at wavelengths λ_2 and λ_6:

$$\alpha_6^2 = \ln\left(\frac{I_2/I_6}{\lambda_6/\lambda_2}\right) , \qquad (1.15)$$

where $\lambda_6 > \lambda_2$ (Jester 2001). The colour-colour diagram is a plot of α_6^2 versus α_{20}^6 for each independent position in the source (separated by a beam width) where λ_2, λ_6 and λ_{20} correspond respectively to wavelengths of 2 cm, 6 cm and 20 cm. Whenever the spectral indices vary across a source (due to synchrotron losses *etc.*), one will observe some locus of points in the colour-colour plane with the shape of the distribution depending on the cause of the spectral variations. With only three well-spaced observations (2 cm, 6 cm and 20 cm) the colour-colour diagram can determine the global shape of the underlying synchrotron spectrum and yield information about the

physics responsible for the spectral variations in the source. A colour-colour diagram for Cygnus A (Fig. 1.1) is shown in Fig. 1.9.

Each point on the colour-colour plane represents information from the wavelengths λ_2, λ_6 and λ_{20}. Katz-Stone et al. (1993) discovered that while each position in Cygnus A has a distinct spectrum from every other position, there exists a unique shift in $\log(I_\nu)$ vs. $\log(\nu)$ space that places each of the spectra on top of one another to surprising accuracy (Fig. 1.10). While Katz-Stone et al. (1993) could not offer a physical justification for these spectral shifts, they argue that since such shifts exist this must point to something fundamental about the underlying physics governing the emission from Cygnus A. The idea of a "universal" spectrum in Cygnus A contrasts the view held by Carilli et al. (1991) that no one spectral model can describe the whole source. In particular, the spectral curvature evident in this diagram is not accounted for by any known analytical model, and this indicates that the physics in Cygnus A is distinct from the physics included in standard synchrotron models (e.g., Fig. 1.5 and Fig. 1.6). This discovery lead Katz-Stone & Rudnick (1994) to develop the physical pair method discussed in the next subsection.

1.3.3 Physical Pair Images

The most basic challenge in understanding extended sources of synchrotron emission is the derivation of physical parameters (such as density and magnetic field distributions) from observations. This is complicated because the synchrotron emissivity depends on a combination of factors, namely: the magnetic field (B), the relativistic
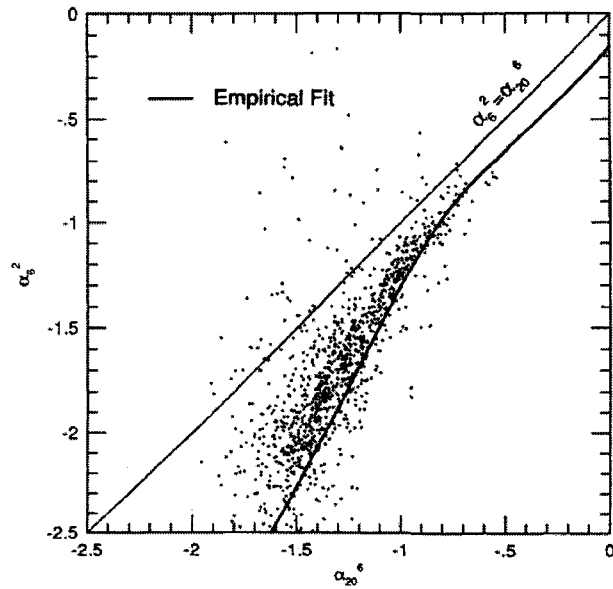
Figure 1.9: Colour-colour diagram (2 cm, 6 cm and 20 cm) for Cygnus A. The lower bold line is the empirical fit to the data (courtesy Katz-Stone et al. 1993).
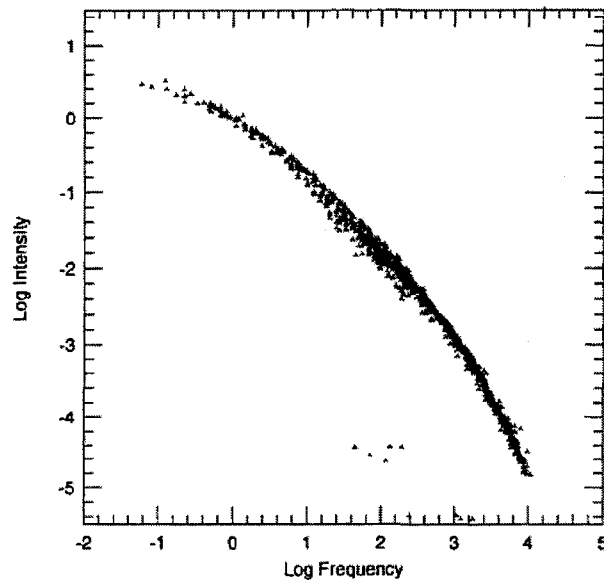
Figure 1.10: "Universal" synchrotron spectrum of Cygnus A generated from multi-frequency observations (courtesy Katz-Stone et al. 1996).

particle energy (E) and the relativistic particle number density (N_T), all of which vary with position in the source and along a given line-of-sight. Katz-Stone and Rudnick (1994) introduce a method of producing frequency independent images that can isolate the relative contributions of the above parameters (when one neglects line-of-sight variations). This is accomplished by utilizing the shape of the relativistic electron energy distribution to modify the total intensity images typically used in analysis of ERS.

In the idealized case where a single power-law spectrum of synchrotron radiation is present throughout the source, it is not possible to isolate the various contributions of N_T, E, and B to the observed emission. When synchrotron losses are present, however, the appearance of the source does change as a function of observing frequency, as shown in Fig. 1.11, making it possible to isolate partially the contributions of the underlying physical parameters.

The electron energy distribution function $N(E)$ [see equation (1.7)] may be re-written as:

$$N(E) \propto \frac{n_T}{E_0} \left(\frac{E}{E_0} \right)^{-x} , \qquad (1.16)$$

where n_T is the number density of relativistic electrons within a given volume and E_0 is a fiducial energy. The synchrotron emissivity, $i(\nu)$ [see equation (1.6)], may then be re-written as:

$$i(\nu) \propto -\frac{\mathrm{d}E}{\mathrm{d}t} \frac{n_T}{E_0} \left(\frac{E}{E_0} \right)^{-x} \frac{\mathrm{d}E}{\mathrm{d}\nu} . \qquad (1.17)$$

Consider the situation where all three variables, B, E, and n_T, are functions of position, $\vec{r}$, in the source. Assuming for the sake of simplicity that $E(\vec{r})$ and $B(\vec{r})$
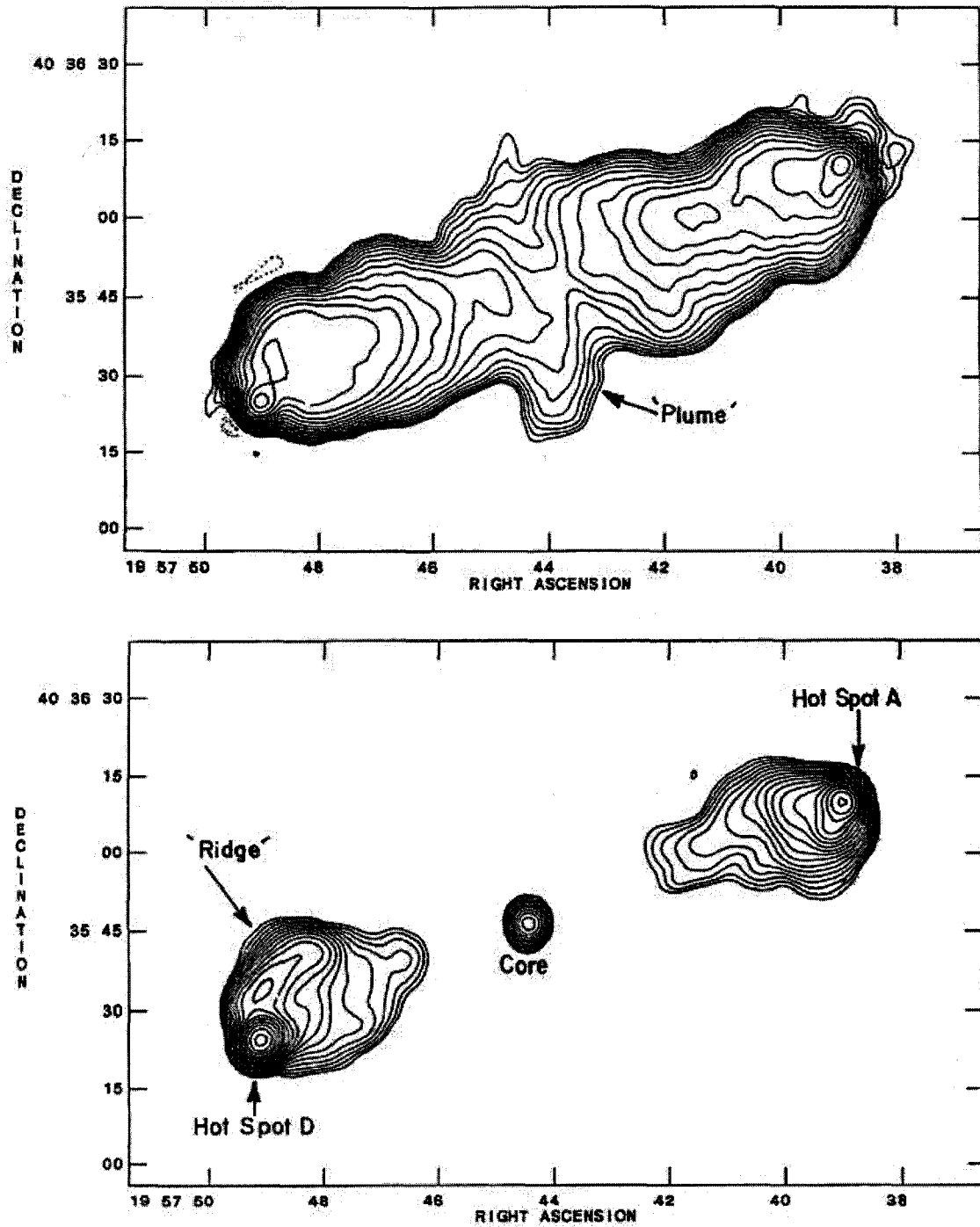
Figure 1.11: (top) Image of Cygnus A at 3.27×10^8 Hz. The contour levels are -1.3, -0.9, 0.9, 1.3, 1.8, 2.5, 3.6, 5.1, 7.2, 10.2, 14.4, 20.4, 28.8, 40.7, 57.6, 81.5, 115, and 163 Jy beam^{-1}. The majority of the emission is from the 'aged' electron populations of the radio lobes. (bottom) Image of Cygnus A at 1.5×10^{10} Hz. The contour levels are -0.05, 0.05, 0.07, 0.1, 0.14, 0.2, 0.28, 0.4, 0.57, 0.8, 1.1, 1.6, 2.3, 3.2, 4.5, 6.4, 9.1, 12.8, and 18.1 Jy beam^{-1}. The majority of the emission is from the 'young' electron populations in the central core and the hot spots (courtesy Carilli et al. 1991).

are uniform along a given line-of-sight path length $L(\vec{r})$, the observed intensity may be written as:

$$I(\nu_{obs}, \vec{r}) \propto i(\nu_{obs}, \vec{r}) \, L(\vec{r}) \, . \tag{1.18}$$

Using equations (1.17), (1.2), (1.4) and (1.5), equation (1.18) may be re-written as:

$$\begin{aligned} I(\nu_{obs}, \vec{r}) \quad &\propto \quad \sqrt{\nu_{obs} B(\vec{r})} \, \frac{n_T(\vec{r})}{E_0(\vec{r})} \, \left(\frac{1}{E_0(\vec{r})} \sqrt{\frac{\nu_{obs}}{B(\vec{r})}} \right)^{-x} L(\vec{r}) \\ &\propto \quad \nu_{obs}^{(1-x)/2} \, B(\vec{r})^{(1+x)/2} \, . \end{aligned}$$

In order to remove the frequency dependence from the observed intensity, the intensity can be calculated not at some fixed observing frequency, ν_{obs}, but at a 'reference' observing frequency, ν_{ref}, which is unique to each position in the source (e.g., the spectral break frequency). Equation (1.4) implies that: $\nu_{br} \propto E_{br}^2 \, B$, where E_{br} is the energy corresponding to the break frequency. Letting the fiducial energy (E_0) be equal to the break energy (E_{br}) and setting $\nu_{br} = \nu_{ref}$ one obtains:

$$\nu_{ref}(\vec{r}) \propto E_0^2(\vec{r}) \, B(\vec{r}) \, . \tag{1.19}$$

Note that equation (1.19) has no dependence on $N_T(\vec{r})$ where $N_T(\vec{r}) \equiv n_T(\vec{r}) L(\vec{r})$. An image of the variations of ν_{ref} across a source directly images the variations of the pair of physical parameters E_0 and B as the product $E_0^2(\vec{r}) \, B(\vec{r})$. This is designated the *first parameter pair image.*

Next, using equation (1.19), the intensity may be written as:

$$I(\nu_{ref}, \vec{r}) \quad \propto \quad \sqrt{\nu_{ref}(\vec{r})B(\vec{r})} \, \frac{n_T(\vec{r})}{E_0(\vec{r})} \, \left(\frac{1}{E_0(\vec{r})} \sqrt{\frac{\nu_{ref}(\vec{r})}{B(\vec{r})}} \right)^{-x} L(\vec{r})$$

$$\propto \quad B(\vec{r}) \, N_T(\vec{r}) \, .$$

The intensity $I(\nu_{ref}, \vec{r})$ is referred to as the 'corrected' intensity and has no dependence on $E_0(\vec{r})$. Since an image of $I(\nu_{ref}, \vec{r})$ maps variations in the pair of variables B and N_T as the product $B(\vec{r}) \, N_T(\vec{r})$, it is designated as the *second parameter pair image*.

The final isolated pair comes from simply dividing the second pair [$B(\vec{r})N_T(\vec{r})$] by the first pair [$E_0^2(\vec{r})B(\vec{r})$]:

$$\frac{N_T(\vec{r})}{E_0^2(\vec{r})} \, , \tag{1.20}$$

and this is the *third parameter pair image*.

Katz-Stone & Rudnick (1994) carried out the above pair imaging procedure using multi-frequency observations of Cygnus A. They set the reference frequency to be the frequency corresponding to a spectral index of $\alpha = 0$ for the "universal" parabolic spectrum shown in Fig. 1.10. Examples of the three pair images for Cygnus A are shown in Fig. 1.12. These images provide a completely new view of Cygnus A and indicate that different physical processes dominate in different regions of ERS. In particular, the hot spots are not seen at all in the BN_T image in stark contrast to traditional total intensity images. The jet is visible in the western lobe of the E_0^2B image, and a channel surrounding the location of the jet is seen in the N_T/E_0^2 image.
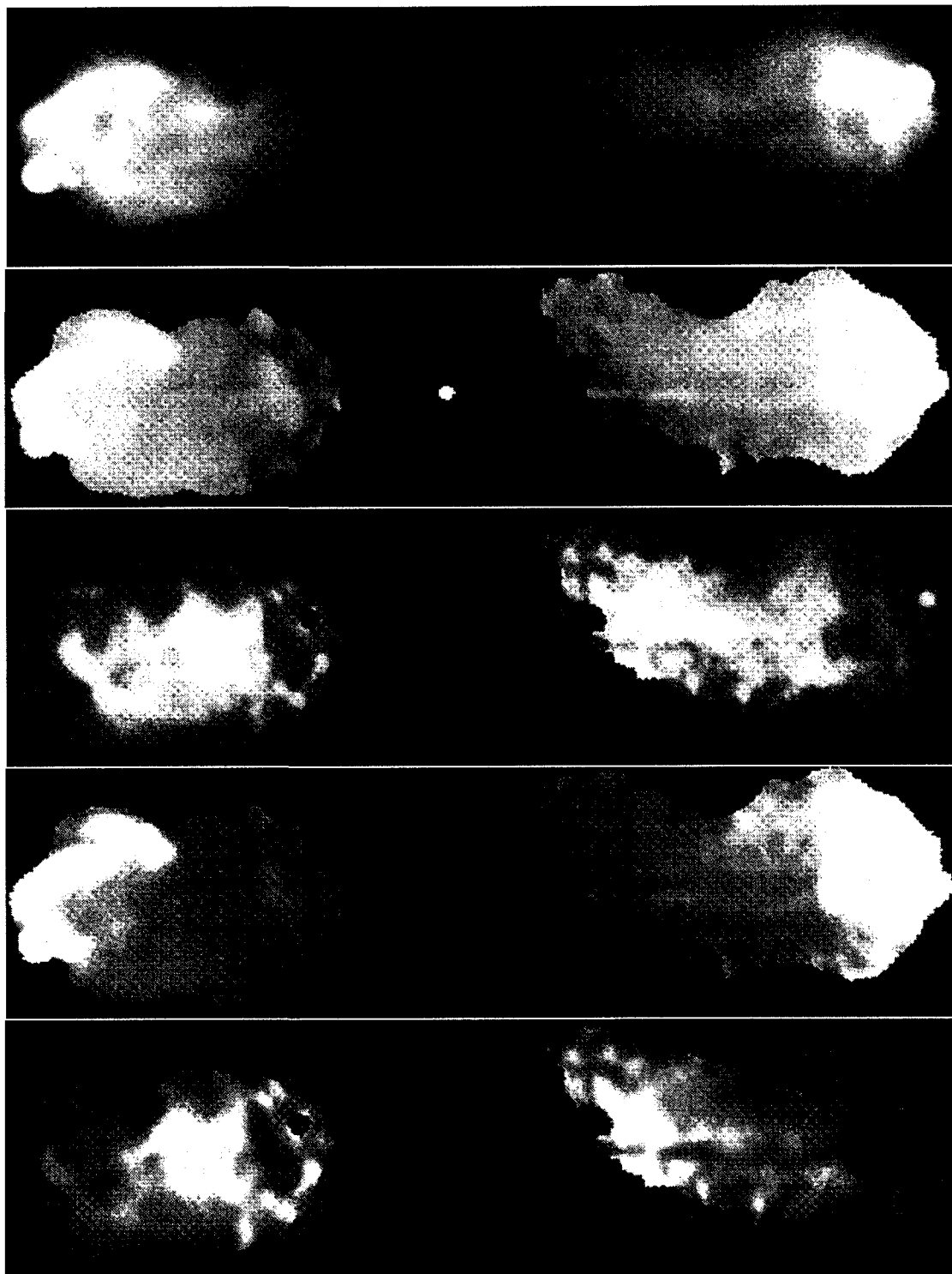
Figure 1.12: (top to bottom) Regular grey-scale intensity image of Cygnus A at 1.4 GHz. Spectral index (α) image of Cygnus A. Corrected intensity image (BN_T). Reference frequency image ($E_0^2 B$). Division of the two previous images (N_T/E_0^2) (courtesy Katz-Stone & Rudnick 1994).

1.4 Numerical Analysis

1.4.1 Previous Work

Magnetic fields are fundamental to the synchrotron mechanism responsible for the radio emission from ERS. Therefore, magnetohydrodynamic (MHD) simulations of ERS form a crucial link between theory and observation. MHD codes use finite difference techniques (Weiss 1983) to solve the following set of coupled partial differential equations:

$$\frac{\partial \rho}{\partial t} + \nabla \cdot (\rho \vec{v}) = 0 \tag{1.21}$$

$$\frac{\partial \vec{s}}{\partial t} + \nabla \cdot (\vec{s}\vec{v}) = -\nabla p + \vec{J} \times \vec{B} \tag{1.22}$$

$$\frac{\partial e}{\partial t} + \nabla \cdot (e\vec{v}) = -p\nabla \cdot \vec{v} \tag{1.23}$$

$$\frac{\partial \vec{B}}{\partial t} = \nabla \times (\vec{v} \times \vec{B}) \,, \tag{1.24}$$

where ρ is the fluid density, $\vec{v}$ is the fluid velocity, $\vec{s} = \rho\vec{v}$ is the momentum density, $\vec{J} = \nabla \times \vec{B}$ is the current density, $\vec{B}$ is the magnetic field, e is the internal energy density, and $p = (\gamma - 1)e$ is the thermal pressure with γ equal to the ratio of specific heats. With the magnetic fields in place, one can set about the task of modeling synchrotron emission. Simulating this emission from the high-energy electrons embedded in ERS flows remains a difficult task numerically. This is because the length and time scales needed to model the microphysics of electron transport are many orders of magnitude smaller than those used in MHD to model the large scale flows of an ERS. In particular, the characteristic diffusion lengths and shock acceleration

times in radio jets are $\leq 1 \ AU$ and $\leq 1 \ yr$ respectively, where as the length and time scales in MHD jet simulations are typically measured in kpc and kyr (Jones et al. 1999). There have been several different numerical schemes implemented over the last twenty years to attempt to bridge this gap.

Clarke, Burns & Norman (1989) computed the first model of synchrotron emission from MHD jet simulations using the ZEUS code. ZEUS-3D (Clarke 1996) is an MHD solver that solves equations (1.21) through (1.24) as functions of three spatial coordinates and time. This emission model, which relies on assumptions about the attributes of the underlying relativistic electron population, was based primarily on the fluid dynamical variables. In particular, the synchrotron emissivity of each computational zone was computed as:

$$i(\nu) = p \ (B \ \sin\!\psi)^{3/2} \ \nu^{-1/2} \ , \qquad (1.25)$$

where ψ is the angle between $\vec{B}$ and a given line-of-sight. The synchrotron emissivities were then integrated along lines of sight through the source yielding measures of the total synchrotron intensity, $I_\nu = \int i(\nu)\mathrm{dl}$. These synchrotron intensities were then projected onto a 2-D radio plane where they were convolved with a Gaussian beam to mimic the resolution of a radio telescope. The drawback of this model is that the non-thermal electron population is not tracked at all and therefore the effects of synchrotron aging and diffusive shock acceleration are not included, resulting in a constant spectral index, α. An example of this technique is shown in Fig. 1.13. This figure shows a line-of-sight integration of synchrotron emissivities computed using
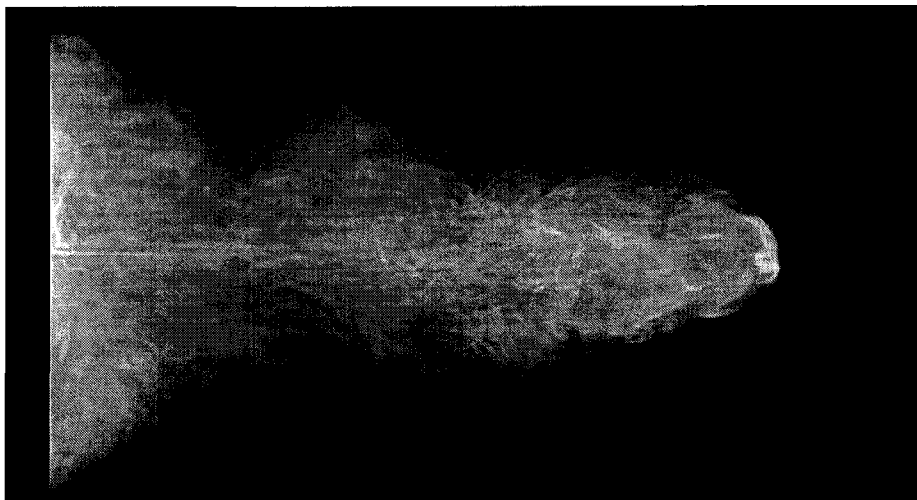
Figure 1.13:   Radio image of a model ERS at 20 cm using the Clarke et al. (1989) emissivity prescription. White/black corresponds to regions of high/low synchrotron emission. The grey scale ranges over four orders of magnitude.

equation (1.25) through a 3-D MHD jet simulation. This line-of-sight integration highlights the filamentary emission from the lobes, but cannot emulate the emission's dependence on frequency (*e.g.* spectral index images) such as that seen in Fig. 1.11.

Matthews & Scheuer (1990) introduced a model in which a non-thermal population of particles is convected 'passively' with the thermal fluid. These particles are subject to synchrotron losses and the effects of adiabatic expansion as they travel along the length of the jet. They assume an electron energy distribution function of the form:

$$dN \propto \Gamma^{-(2\alpha+1)} \, d\Gamma \, , \tag{1.26}$$

where $\alpha \sim 1$ and dN is the number of particles with a Lorentz factor between Γ and $\Gamma + d\Gamma$. This initial power-law distribution is then subjected to the effects of adiabatic expansion and synchrotron losses yielding the following modified energy distribution

function:

$$dN \propto \Gamma^{-(2\alpha+1)}(1 - bR\Gamma)^{2\alpha-1} \, d\Gamma \, , \tag{1.27}$$

where b is a synchrotron loss parameter and R is an adiabatic expansion factor. The synchrotron emissivity of each zone is:

$$i \propto \int_0^\infty N(\Gamma)d\Gamma \, . \tag{1.28}$$

As before, these emissivities are integrated along a given line of sight to yield the total synchrotron intensity (I_ν). While this model treats the number density of the relativistic particles more realistically than Clarke et al. (1989), it does not include the effects of diffusive shock acceleration nor does it give a proper MHD treatment of the magnetic field.

Massaglia et al. (1995) modeled radiative effects in their 'pseudo' MHD jet simulations by following the temporal evolution of a distribution of 'test' particles subject to synchrotron losses, adiabatic expansion and shock acceleration. To follow the test particles they solved an additional advection equation for the scalar ζ:

$$\frac{\partial \zeta}{\partial t} + (\vec{v} \cdot \nabla)\zeta = 0 \, , \tag{1.29}$$

where the initial jet and ambient values were set to $\zeta = 1$ and $\zeta = 0$ respectively. This scalar allows the authors to distinguish between fluid which is initially injected through the jet and fluid which forms the surrounding ambient medium. From Kardashev (1962), the evolution equation of a population of relativistic electrons can be

written as:

$$\frac{DN}{Dt} = \frac{\partial}{\partial E}[\ (-\sigma E + \beta E^2)N\ ]\ , \tag{1.30}$$

where N is the electron energy distribution function, $\sigma = -\nabla \cdot \vec{v}/3$ and $\beta \propto B^2$. The first term on the right hand side of equation (1.30) accounts for adiabatic expansion and the second term for synchrotron losses. Solving equation (1.30) yields the following expression for the temporal evolution of the distribution function:

$$N(E,t) = \kappa E^{-x}[\ 1 - Ee^{-a_2}a_1\ ]^{x-2}e^{(x-1)a_2}\ , \tag{1.31}$$

where

$$N(E,0) = \kappa_0 E^{-x}\ ,\quad a_1 = \int_0^t \beta e^{a_2}dt\ ,\quad a_2 = \int_0^t \sigma dt\ .$$

The integrals for a_1 and a_2 are evaluated following the trajectory of an individual fluid element yielding two additional evolution equations which are solved alongside the other fluid equations. In order to model shock acceleration in 'strong' shocks (with a pressure jump ≥ 2) the authors assume that the test particle energy is increased by a factor which is proportional to the shock strength. Their simulations showed that a filamentary structure developed in the break frequency distribution with high break frequency concentrations located in the shocked regions of the flow and in the initial part of the jet where young material, unaffected by synchrotron losses, entered the grid. As with the Matthews & Scheuer model, however, a proper MHD treatment of the magnetic fields was not implemented.

Jones, Ryu & Engel (1999) and Tregillis, Jones & Ryu (2001) have developed a numerical algorithm that explicitly simulates the time-dependent transport of relativistic electrons in 2-D and 3-D MHD jet simulations. Their numerical scheme includes, self-consistently, the effects of synchrotron aging, adiabatic expansion and diffusive shock acceleration. This electron transport scheme utilizes a modified form of the standard diffusion-convection equation (Skilling 1975):

$$\frac{\partial f}{\partial t} = \frac{1}{3}\, p\, \frac{\partial f}{\partial p}\, (\nabla \cdot \vec{v}) - \vec{v} \cdot \nabla f + \nabla \cdot (\lambda \nabla f) + \frac{1}{p^2}\, \frac{\partial}{\partial p} \left(p^2 D \frac{\partial f}{\partial p} \right) + Q \ , \qquad (1.32)$$

where $f(\vec{r}, p, t)$ is the isotropic part of the nonthermal electron distribution, λ is a spatial diffusion coefficient, D is a momentum diffusion coefficient, Q is a source term that represents the net effects of injection and synchrotron losses at a given momentum, p, and $\vec{v}$ is the thermal plasma velocity.

Under the assumption that the dynamical feedback of the high-energy electron population can be ignored, the authors are able to create a simplified numerical scheme that still correctly captures the physics of electron transport present in equation (1.32). Their algorithm is divided into two separate numerical schemes: one for shocks and the other for smooth flows. Since the electron transport time step is many orders of magnitude smaller than the numerical time step, the authors argue that it is not necessary to model the detailed time evolution of $f(\vec{r}, p, t)$ across shocks. Instead, they assume that $f(\vec{r}, p, t)$ is broad enough that it can be approximated by a power-law over a finite number of momentum bins (see Kang & Jones 1991, 1995,

1997). Therefore, immediately downwind of a shock $f \propto p^{-q}$, where q is a momentum index. The spectral index α is related to q such that $\alpha = (q-3)/2$.

The authors divide the momentum range of interest into N logarithmically spaced bins bounded by p_o and p_N. In particular, for their 3-D calculations: $p_0 = 10 \; m_e c$ and $p_N = 1.63 \times 10^5 \; m_e c$ with $N = 8$. This momentum range is representative of the post shock energies at which electrons are believed to be injected at shocks in non-relativistic jets. Thus, the computational effort required for this scheme amounts to adding eight variables to an MHD scheme, effectively doubling the time required for a solution.

In addition to transporting electrons, this model injects electrons at shocks using a common injection model. A fixed fraction of the total electron flux through a shock is injected and accelerated to the appropriate power-law momentum distribution. These initial post-shock momentum distributions then evolve in time owing to synchrotron and expansion losses in the smooth flows downwind of the shocks.

A 3-D numerical jet simulation that incorporated the above electron transport scheme was carried out on a uniform grid consisting of $576 \times 192 \times 192$ computational zones. The synchrotron emissivity, which is dependent upon the spatial distributions of f, p and q in this scheme, was computed in each zone:

$$i(\nu) \propto f(p) \; p^q \; \nu^{-\alpha}. \tag{1.33}$$

Line-of-sight integrations of these emissivities were carried out generating the radio image shown in Fig. 1.14.
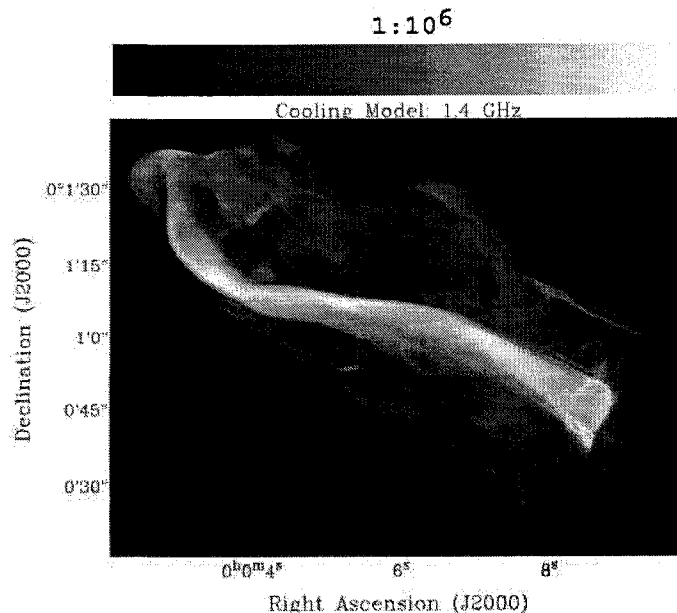
Figure 1.14: Synthetic synchrotron intensity image calculated at $\nu = 1.4$ GHz. (courtesy Tregillis et al. 2001).

The jet and its surrounding lobe are clearly visible, along with several regions of enhanced emission in the head region. Previously, semi-empirical prescriptions for the synchrotron emissivity did not produce the visible jet structure that is evident in this radio image.

1.4.2 Scope of this Thesis

The body of this thesis will present an extension to the semi-empirical model developed by Clarke, Burns & Norman (1989) for the purpose of simulating synchrotron emission from MHD calculations of ERS. The Tregillis et al. (2001) assumption of an underlying power-law momentum distribution is taken a step further. It is assumed that these power-laws can be modeled by a single 3-D scalar instead of 8 momentum bins. This assumption makes the numerical treatment of synchrotron intensity

significantly simpler than the above algorithms and less computationally intensive. This new algorithm still successfully models the synchrotron emission and produces radio images qualitatively similar to those shown in Fig. 1.14. In particular, the synchrotron age (t_{syn}) of a relativistic population of electrons embedded in an MHD fluid can be tracked with the addition of a single 3-D scalar. When combined with the magnetic field (B), the density (ρ) and the internal energy (e), this new scalar allows computation of a full suite of synthetic multi-frequency radio observations at relatively low computational cost.

The ZEUS-3D code is used to compute a full 3-D model of an MHD jet and then the observational analyses proposed by Katz-Stone & Rudnick (1996), namely: colour-colour diagrams, tomography imaging and physical pair imaging, are carried out using synthetic observations. Direct comparisons between the synthetic images produced and those derived from multi-frequency observations of Cygnus A by Katz-Stone & Rudnick (1996) are made, and for the first time the assumptions made in §1.3.3 about line-of-sight variations in ERS are tested.

Chapter 2

Methodology

2.1   Synchrotron Aging and Shock Acceleration

In order to simulate the synchrotron emissivity of the plasma, the synchrotron age of

the fluid (t_{syn}) is tracked using the following advection equation:

$$\frac{\partial t_{\mathrm{syn}}}{\partial t} + \vec{v} \cdot \nabla t_{\mathrm{syn}} = 1 - \xi\, t_{\mathrm{syn}} \;, \tag{2.1}$$

where the first term on the right hand side of equation (2.1) accounts for synchrotron

aging and the second term for shock re-acceleration. The 'aging' source term in-

creases the synchrotron age of the fluid with the time step, the effect of which is to

gradually drive ν_{br} to lower frequencies. In contrast, the 'shock' source term re-sets

the synchrotron age to smaller values driving ν_{br} back to higher frequencies. It is the

combination of these two source terms that creates the spectral evolution modeled

by this algorithm. The $\vec{v} \cdot \nabla t_{\mathrm{syn}}$ term on the left hand side of equation (2.1) corre-

sponds to an "advection term" and is handled by the existing "machinery" in the

ZEUS-3D code, namely the transport step. In particular, equation (2.1) is solved in

an operator-split fashion:

$$\frac{\partial t_{\text{syn}}}{\partial t} + \vec{v} \cdot \nabla t_{\text{syn}} = 0$$

$$\Rightarrow \rho \left[\frac{\partial t_{\text{syn}}}{\partial t} + \vec{v} \cdot \nabla t_{\text{syn}} \right] + t_{\text{syn}} \left[\frac{\partial \rho}{\partial t} + \vec{v} \cdot \nabla \rho \right] = 0$$

$$\Rightarrow \frac{\partial \rho t_{\text{syn}}}{\partial t} + \vec{v} \cdot \nabla \rho t_{\text{syn}} = 0$$

and thus ρt_{syn} is solved like the continuity equation [see equation (1.21)].

Next, the source terms are accounted for using the Lagrangian form of equation (2.1):

$$\frac{\mathrm{d} t_{\text{syn}}}{\mathrm{d} t} = 1 - \xi \, t_{\text{syn}} \, . \tag{2.2}$$

The reader is reminded that the Lagrangian derivative, $\frac{\mathrm{d}}{\mathrm{d}t}$, is related to the Eulerian derivative, $\frac{\partial}{\partial t}$, as follows: $\frac{\mathrm{d}}{\mathrm{d}t} = \frac{\partial}{\partial t} + \vec{v} \cdot \nabla$.

An expression for the dependence of the synchrotron age on the break energy, E_{br}, may be obtained by combining equations (1.4) and (1.12) yielding (mks units):

$$t_{\text{syn}} = 3.1682 \times 10^{-13} \, B^{-2} \, E_{\text{br}}^{-1} \, . \tag{2.3}$$

To find ξ in terms of the flow variables, the assumption that $E_{\text{br}} \propto e/\rho$, the specific internal energy (temperature), is made and thus across a shock:

$$\frac{E_{\text{br}}'}{E_{\text{br}}} = \frac{(e/\rho)'}{(e/\rho)} \, , \tag{2.4}$$

where the $'$ denotes the post-shock values. This is a reasonable assumption since the

energy of the relativistic particles embedded in an MHD flow should be a monotonic function of the fluid temperature. It follows from equations (2.3) and (2.4) that the ratio of the post to pre-shock synchrotron age is:

$$\frac{t'_{\text{syn}}}{t_{\text{syn}}} = \frac{B^2}{B'^2} \frac{E_{\text{br}}}{E'_{\text{br}}} = \frac{B^2}{B'^2} \frac{e}{e'} \frac{\rho'}{\rho} \equiv \zeta < 1 \Rightarrow t'_{\text{syn}} = \zeta \, t_{\text{syn}} \, . \qquad (2.5)$$

It then follows that the second source term in equation (2.2) is given by:

$$\frac{t'_{\text{syn}} - t_{\text{syn}}}{\text{d}t} = -\frac{(1-\zeta)}{\text{d}t} \, t_{\text{syn}} \Rightarrow \xi = \frac{(1-\zeta)}{\text{d}t} \, . \qquad (2.6)$$

In order to derive expressions for the ratios in ζ, one can make use of the Lagrangian forms of the continuity, internal energy and induction equations. Thus, in the Lagrangian frame, the continuity equation [see equation (1.21)] can be written as:

$$\frac{\text{d}\rho}{\text{d}t} = -\rho \nabla \cdot \vec{v} \Rightarrow \text{d}\rho = -\rho \nabla \cdot \vec{v} \, \text{d}t \, . \qquad (2.7)$$

If one takes the post shock density, ρ', to be $\rho' = \rho + \text{d}\rho$ and substitutes the above expression for $\text{d}\rho$ using the 'time centred' value for ρ on the right hand side one obtains:

$$\rho' = \rho - \left(\frac{\rho + \rho'}{2}\right) \nabla \cdot \vec{v} \, \text{d}t \qquad (2.8)$$

$$\Rightarrow \frac{\rho'}{\rho} = \frac{(1 - \nabla \cdot \vec{v} \, \text{d}t/2)}{(1 + \nabla \cdot \vec{v} \, \text{d}t/2)} \, . \qquad (2.9)$$

Similarly, the internal energy equation [see equation (1.23)] in the Lagrangian frame is:

$$\frac{\mathrm{d}e}{\mathrm{d}t} = -\gamma e \nabla \cdot \vec{v} \Rightarrow \mathrm{d}e = -\gamma e \nabla \cdot \vec{v}\,\mathrm{d}t\ .$$

Taking the post shock internal energy density to be $e' = e + \mathrm{d}e$ and substituting the above expression for $\mathrm{d}e$ using the 'time centred' value for e on the right hand side one obtains:

$$e' = e - \gamma\left(\frac{e+e'}{2}\right)\nabla \cdot \vec{v}\,\mathrm{d}t \qquad (2.10)$$

$$\Rightarrow \frac{e'}{e} = \frac{(\,1 - \gamma\nabla \cdot \vec{v}\,\mathrm{d}t/2\,)}{(\,1 + \gamma\nabla \cdot \vec{v}\,\mathrm{d}t/2\,)}\ . \qquad (2.11)$$

Finally, the Lagrangian form of the induction equation [see equation (1.24)] can be written as:

$$\frac{\mathrm{d}\vec{B}}{\mathrm{d}t} = (\vec{B}\cdot\nabla)\vec{v} - \vec{B}(\nabla\cdot\vec{v})\ ,$$

having used the vector identity $\nabla\times(\vec{v}\times\vec{B}) = (\vec{B}\cdot\nabla)\vec{v} - (\vec{v}\cdot\nabla)\vec{B} - \vec{B}(\nabla\cdot\vec{v}) + \vec{v}(\nabla\cdot\vec{B})$, the solenoidal condition ($\nabla\cdot\vec{B} = 0$), and the definition of the Lagrangian derivative. Taking the 'dot product' with $\vec{B}$ one obtains:

$$\vec{B}\cdot\frac{\mathrm{d}\vec{B}}{\mathrm{d}t} = \frac{1}{2}\frac{\mathrm{d}B^2}{\mathrm{d}t} = \vec{B}\cdot[\,(\vec{B}\cdot\nabla)\vec{v} - \vec{B}(\nabla\cdot\vec{v})\,] \Rightarrow \mathrm{d}B^2 = 2B^2(\chi - \nabla\cdot\vec{v})\,\mathrm{d}t\ , \quad (2.12)$$

where $\chi \equiv \hat{B}\cdot(\hat{B}\cdot\nabla)\vec{v}$, and where $\hat{B} = \vec{B}/B$ is a unit vector parallel to $\vec{B}$.

Taking the square of the post shock magnetic field intensity to be $B'^2 = B^2 + \mathrm{d}B^2$ and substituting the above expression for $\mathrm{d}B^2$ using the 'time centred' value for B^2 on the right hand side one obtains:

$$B'^2 = B^2 + 2\left(\frac{B^2 + B'^2}{2}\right)(\chi - \nabla \cdot \vec{v})\,\mathrm{d}t \qquad (2.13)$$

$$\Rightarrow \frac{B^2}{B'^2} = \frac{1 - (\chi - \nabla \cdot \vec{v})\,\mathrm{d}t}{1 + (\chi - \nabla \cdot \vec{v})\,\mathrm{d}t}. \qquad (2.14)$$

In this fashion the jumps in ρ, e and B^2, all of which are required to evaluate ζ, have been related to two locally determinable quantities, namely, $\nabla \cdot \vec{v}$ and χ. While $\nabla \cdot \vec{v}$ is straightforward to evaluate, χ is much more challenging, and the reader is referred to Appendix A for details.

With ζ now known, the age update can be evaluated in the Lagrangian frame. Substituting equation (2.6) into equation (2.2) yields:

$$\frac{\mathrm{dt}_{\mathrm{syn}}}{\mathrm{dt}} = 1 - \frac{(1 - \zeta)}{\mathrm{dt}}\,t_{\mathrm{syn}}$$

$$\mathrm{dt}_{\mathrm{syn}} = \mathrm{d}t - (1 - \zeta)t_{\mathrm{syn}}$$

$$\Rightarrow t'_{\mathrm{syn}} = t_{\mathrm{syn}} + \mathrm{dt}_{\mathrm{syn}}$$

$$= t_{\mathrm{syn}} + \mathrm{d}t + (\zeta - 1)t_{\mathrm{syn}}.$$

This completes the age update when both the effects of synchrotron aging and shock acceleration are included.

$$\rho', v', p' \longrightarrow \qquad \xrightarrow[V]{} \qquad \longleftarrow \rho, v, p$$

post-shock   shock   pre-shock
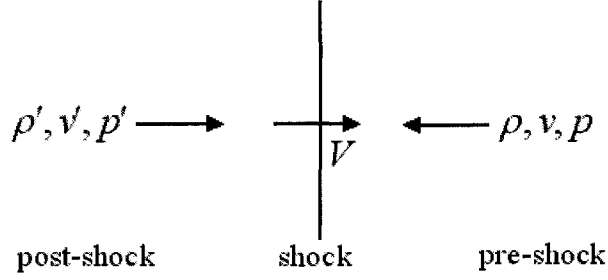
Figure 2.1: A strong shock moving with speed V.

2.2 Shock Limiters

A shock moving with speed V is depicted in Fig. 2.1. The post-shock variables are denoted as (ρ', v', p') and the pre-shock variables as (ρ, v, p). Diffusive shock acceleration only occurs in strong shocks where $p'/p \equiv \varpi \geq 2$ (Jones et al. 1999). The shock algorithm developed is dependent upon the velocity divergence $(\nabla \cdot \vec{v})$, the time step (dt), and the scalar χ, none of which directly discriminates between strong shocks and weak shocks. Therefore, a shock 'limiter' is required to ensure that the shock portion of the algorithm is applied only in computational zones where a strong shock exists.

The velocity divergence, $\nabla \cdot \vec{v}$, is calculated in each zone and is the principal measure of shock strength in the code. A limiter divergence, $\nabla \cdot \vec{v}_{\text{lim}}$, is also computed and is defined to be the minimum shock strength necessary to re-energize the fluid in each particular zone. A comparison between these two shock measures is made every time-step. If the local $\nabla \cdot \vec{v}$ is greater than the limiter, the shock source term is applied in that zone.

The velocity divergence may be written in Cartesian coordinates as:

$$\nabla \cdot \vec{v} = \partial_x v_x + \partial_y v_y + \partial_z v_z \ . \tag{2.15}$$

In numerical MHD schemes a shock is not modeled as a perfect discontinuity but is 'smeared' out over several computational zones. The factor q_{con} is a tunable parameter in the ZEUS-3D code that governs the level of numerical diffusion permitted when modeling shocks. q_{con} is roughly equal to two less than the number of zones over which a shock is smeared. Thus, for $q_{\mathrm{con}} \sim 2$, one can expect roughly 4 zones across a shock. When this numerical diffusion is accounted for in the difference form of equation (2.15), one obtains:

$$\nabla \cdot \vec{v} = \frac{v_x' - v_x}{(q_{\mathrm{con}} + 2)\delta_x} + \frac{v_y' - v_y}{(q_{\mathrm{con}} + 2)\delta_y} + \frac{v_z' - v_z}{(q_{\mathrm{con}} + 2)\delta_z} \ , \tag{2.16}$$

where δ_x, δ_y and δ_z are the zone dimensions in the $\hat{x}$, $\hat{y}$ and $\hat{z}$ directions respectively. Across a strong shock the velocity difference in each of the three directions is:

$$v_n' - v_n = -\frac{2c_s(\varpi - 1)}{\sqrt{2\gamma(\gamma - 1)(1 + \beta\ \varpi)}} \ , \tag{2.17}$$

where c_s is the pre-shock sound speed, γ is the adiabatic index, $\beta = (\gamma + 1)/(\gamma - 1)$ and $n = x, y, z$. Substituting equation (2.17) into equation (2.16) yields:

$$\nabla \cdot \vec{v} = -\frac{2c_s(\varpi - 1)}{\sqrt{2\gamma(\gamma - 1)(1 + \beta\varpi)}} \frac{1}{(q_{\mathrm{con}} + 2)} \left(\frac{1}{\delta_x} + \frac{1}{\delta_y} + \frac{1}{\delta_z}\right) \ . \tag{2.18}$$

It is assumed that the pre-shock sound speed in equation (2.18) is roughly equal to the local sound speed in each computational zone: $c_s \sim c(i,j,k)$. For the shock range of interest this is a reasonable assumption. As proof, consider that:

$$c_s^2 \equiv \frac{\gamma p}{\rho} \,, \tag{2.19}$$

and therefore, substituting $p' = \varpi p$ yields:

$$c_s'^2 - c_s^2 = \gamma \left(\frac{p'}{\rho'} - \frac{p}{\rho} \right) = c_s^2 \left(\varpi \frac{\rho}{\rho'} - 1 \right) \,. \tag{2.20}$$

The density jump ρ/ρ' is related to the pressure jump ϖ through: $\rho/\rho' = (\beta+\varpi)/(1+\beta\varpi)$. It then follows from equation (2.20) that the fractional change in sound speed across a strong shock is:

$$\frac{c_s'^2 - c_s^2}{c_s^2} = \varpi \left(\frac{\beta + \varpi}{1 + \beta\varpi} \right) - 1 \,. \tag{2.21}$$

For $\varpi = 2$ and $\gamma = 5/3$ ($\beta = 4$), equation (2.21) yields: $(c_s'^2 - c_s^2)/(c_s^2) = 1/3$ and therefore the assumption that $c_s \sim c_s' \sim c(i,j,k)$ is justified.

The following divergence limiter is computed in each zone:

$$\nabla \cdot \vec{v}_{\text{lim}}(i,j,k) = -\frac{2\,c(i,j,k)\,(\varpi - 1)}{\sqrt{2\gamma(\gamma-1)(1+\beta\varpi)}} \frac{1}{(q_{\text{con}}+2)} \left(\frac{1}{\delta_x(i)} + \frac{1}{\delta_y(j)} + \frac{1}{\delta_z(k)} \right) \,. \tag{2.22}$$
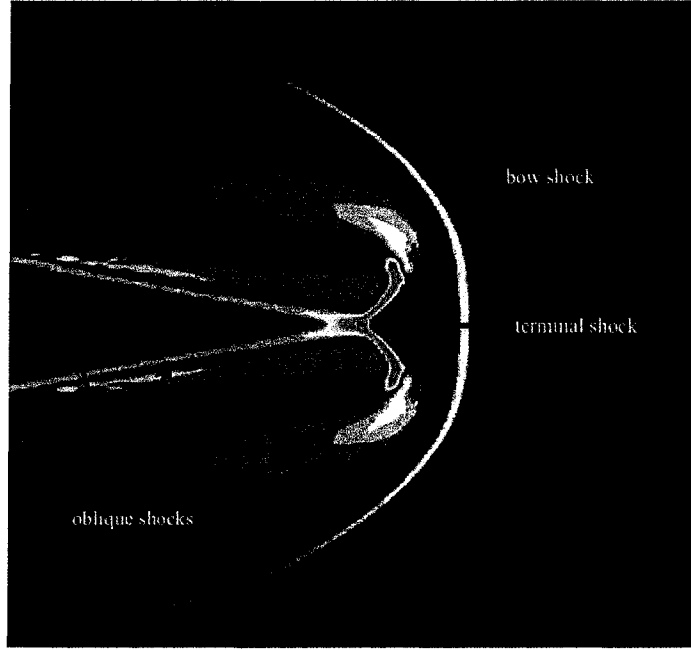
Figure 2.2: Contour plot of the velocity divergence ($\nabla \cdot \vec{v}$) illustrating the initial shock structure.

If $\nabla \cdot \vec{v} \ (i,j,k) \geq \nabla \cdot \vec{v}_{\text{lim}}(i,j,k)$ the shock source term is applied; otherwise the fluid

is simply aged:

$$t'_{\text{syn}} = \begin{cases} t_{\text{syn}} + \mathrm{d}t & \nabla \cdot \vec{v} \ (i,j,k) < \nabla \cdot \vec{v}_{\text{lim}}(i,j,k) \\[2ex] t_{\text{syn}} + \mathrm{d}t + (\zeta - 1)t_{\text{syn}} & \nabla \cdot \vec{v} \ (i,j,k) \geq \nabla \cdot \vec{v}_{\text{lim}}(i,j,k) \ . \end{cases} \tag{2.23}$$

A test of this shock limiter was carried out. A 2-D calculation of the initial stages

of a jet propagating into a uniform ambient medium was run using the ZEUS-3D

code. Three separate shocks formed: an oblique shock along the length of the jet, a

terminal shock in the head region of the jet and a bow shock in the ambient medium

(Fig. 2.2). A plot of the pressure (Fig. 2.3) indicates that the pressure jump across

the oblique shock is ~ 3. The pressure ratio term ϖ was initially set to 2 in equation

(2.22), which should include the oblique shock, and then it was set to 4, which should
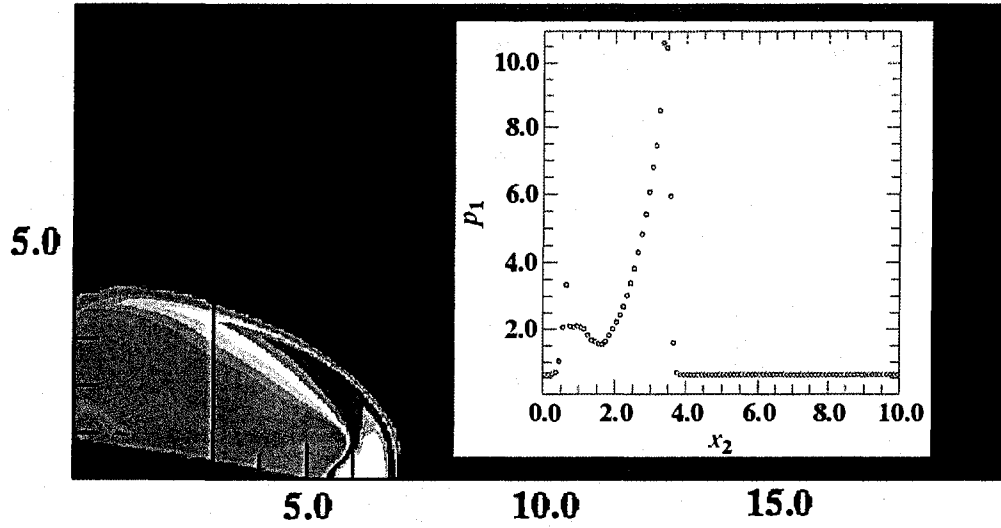
Figure 2.3: Contour plot of the pressure. A 1-D slice is indicated on the contour plot and is shown to the right.

exclude the oblique shock. The results of this test are shown in Fig. 2.4. In the first case, the shock ratio term ζ [see equation(2.5)] is computed along the entire length of the oblique shock, whereas in the second case the majority of the oblique shock is excluded. This test confirms that the shock limiter correctly discriminates the various shock strengths present in the numerical simulations.

2.3 Test Models and Lagrangian Tracers

Two test simulations were carried out, using the ZEUS-3D code, to illustrate the effects of the aging and shock source terms. The simulations were run on a 2-D grid $(305 \times 165$ zones) into which a Mach 10, underdense jet $(\eta = \rho_j/\rho_a = 0.01)$ with a trace toroidal magnetic field was launched. The first simulation, the 'aging' model, included only the aging source term while the second simulation, the 'shock' model,
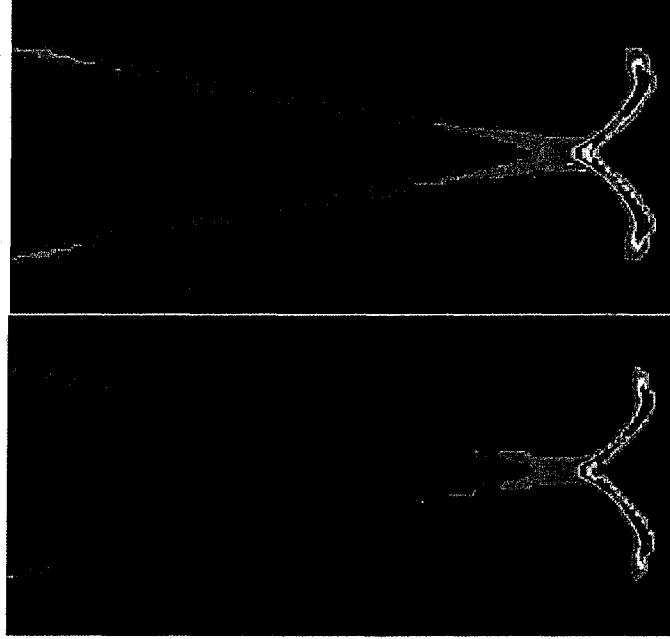
Figure 2.4: Contour plots of the shock ratio term (ζ) for $\varpi = 2$ (top) and for $\varpi = 4$ (bottom).

included both the aging and shock source terms. Fig. 2.5 shows the synchrotron age distribution at the end of the 'aging' simulation. One can see that the synchrotron age of the fluid gradually increases along the length of the jet and then back into the lobes. In contrast, Fig. 2.6 shows the synchrotron age distribution at the end of the 'shock' simulation. The main difference between the two age distributions is the existence of a region of extremely 'young' material at the terminal point of the jet in the 'shock' model. This region of 'young' synchrotron age is co-spatial with the terminal shock of the jet shown in Fig. 2.7. This illustrates the algorithm's ability to re-energize the fluid in the regions of strong shocks.
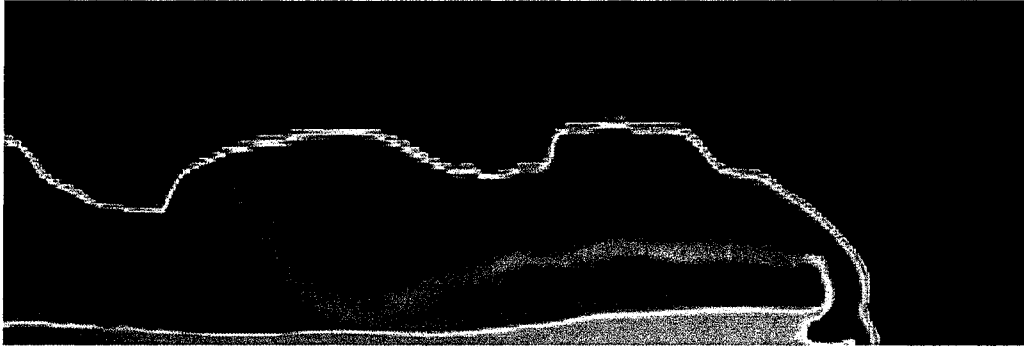
Figure 2.5: Synchrotron age distribution of the 'aging' model. Blue/red corresponds to regions of young/old material.
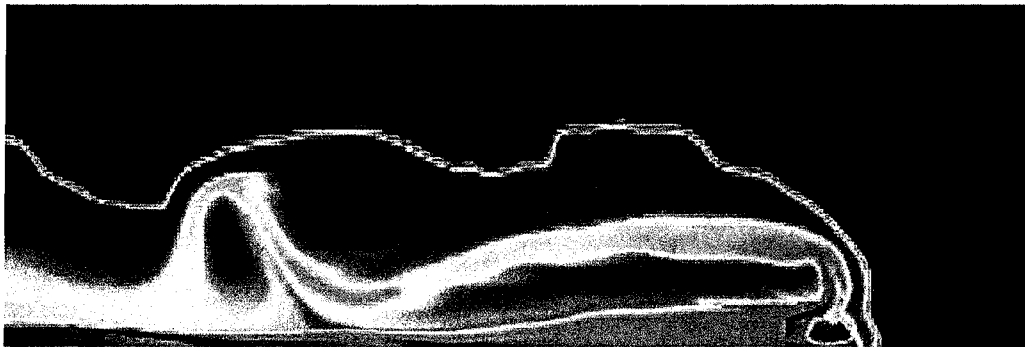
Figure 2.6: Synchrotron age distribution of the 'shock' model. Blue/red corresponds to regions of young/old material.
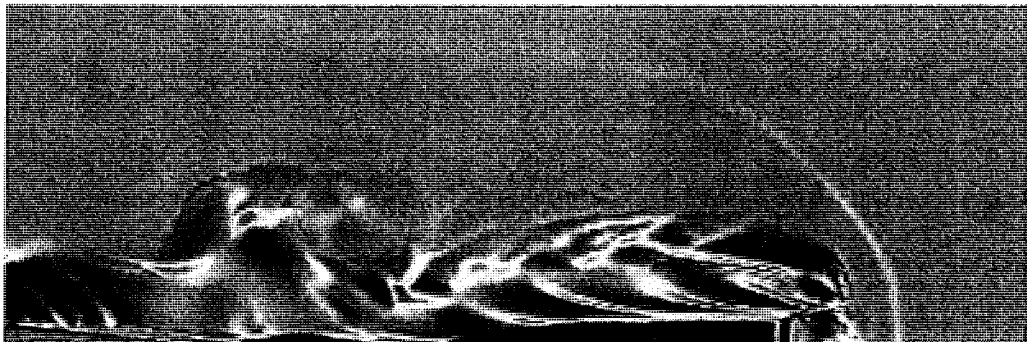
Figure 2.7: Velocity Divergence distribution of the jet model. Blue/red corresponds to regions of shocked $(\nabla \cdot \vec{v} < 0)$/rarefied $(\nabla \cdot \vec{v} > 0)$ material. The terminal shock is the dark blue feature at the extreme right of the jet in this image.

To further investigate the functionality of this new algorithm, Lagrangian tracers were introduced into the code to monitor both the synchrotron age and the velocity divergence of the fluid through the course of the simulation. Since the code is Eulerian by design, it is unable to provide detailed information about the physical conditions that an individual element of fluid experiences during its passage through the jet. The tracers, therefore, act as probes moving along with the flow recording the physical conditions they encounter.

Each tracer's position is updated using the following prescription:

$$x_n^{\text{new}} = x_n^{\text{old}} + v_n^{\text{ave}} \mathrm{d}t \ , \tag{2.24}$$

where $n = x, y, z$ and v_n^{ave} is the average of the local velocity interpolated to the tracer's position. The velocities, along with any other variables the tracers are instructed to monitor, are interpolated to the tracer's position using a simple linear interpolation scheme (in 1-D $\rightarrow n = x$):

$$v_x^{\text{ave}} = \frac{r(i)v_x(i+1) + r(i+1)v_x(i)}{r(i) + r(i+1)} \ , \tag{2.25}$$

where $r(i)$ and $r(i+1)$ are the distances of the tracer from the ith and the $i^{\text{th}} + 1$ zone centres. The 1-D interpolation scheme given in equation (2.25) has been expanded for use in three dimensions and is implemented in the code. After the tracer positions are updated in each time-step, a record of these interpolated quantities is stored in a file producing a tracer 'history' of each variable. These quantities can be plotted as a
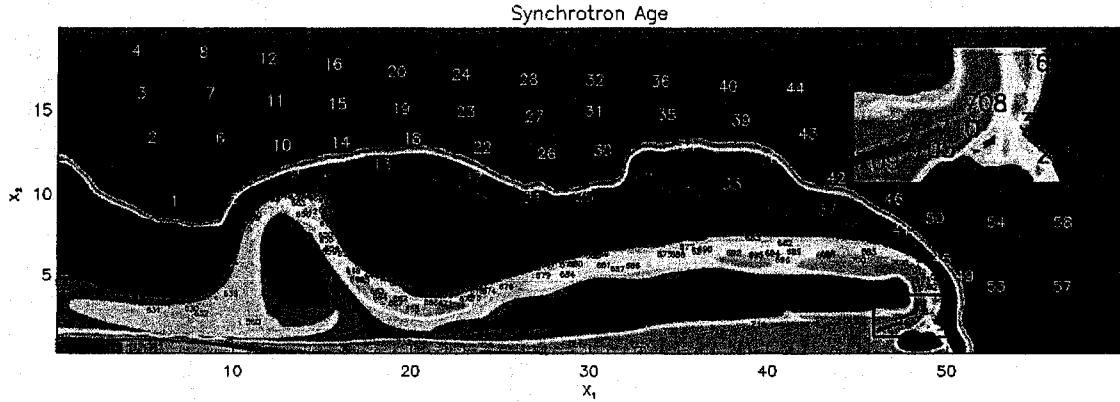
Figure 2.8: Positions of ambient tracers (white) and jet tracers (blue) overlaid on the synchrotron age distribution of the 'shock' model.

function of time. For the jet simulations examined, two sets of tracers were introduced into the code. A lattice of 'ambient' tracers is placed in the ambient medium and a secondary set of 'jet' tracers is carried into the grid with the jet flow (Fig. 2.8).

As a test of the shock algorithm, the tracers monitored both the synchrotron age and velocity divergence during the simulation. In particular, the aim of this test is to ensure that as the fluid repeatedly encounters 'strong' shocks throughout the course of the simulation, the synchrotron ages of the fluid are re-set accordingly. Tracer histories of the synchrotron age and the shock ratio term ζ are shown in Fig. 2.9. The shock ratio term ζ is set to zero by default and is only computed when a strong shock is encountered $[\nabla \cdot \vec{v}\,(i,j,k) \geq \nabla \cdot \vec{v}_{\text{lim}}(i,j,k)]$. This particular tracer passed through four separate 'strong' shocks which result in four separate 'reductions' in the synchrotron age. This tracer history confirms that the algorithm is correctly applying the source terms in equation (2.2).
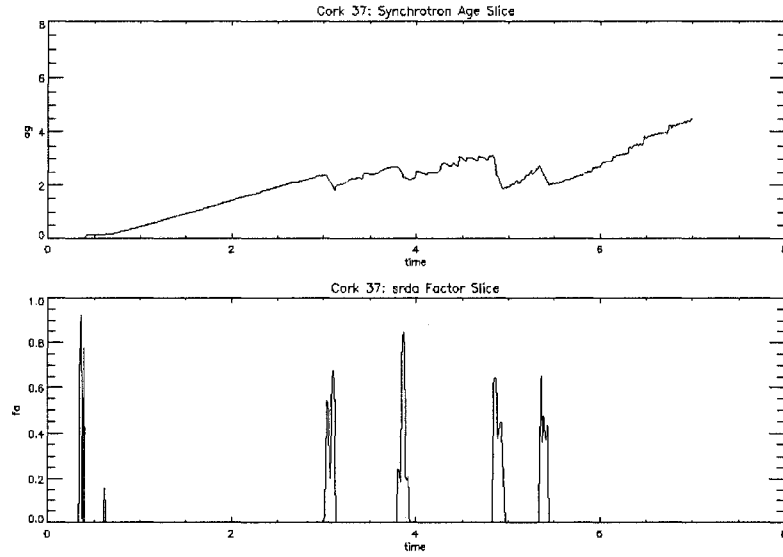
Figure 2.9: Histories of the synchrotron age t_{syn} (top) and the shock ratio term ζ (bottom) for a Lagrangian tracer in the jet. Note that this particular tracer passed through four shocks after $t = 2$, each resulting in a spike in ζ in the bottom panel and a reduction of "age" in the top panel. The spike in ζ at $t = 0.3$ corresponds to when this tracer was launched. Thus, $t_{\text{syn}} \sim 0$, and no reduction of age was possible.

2.4 Synchrotron Emissivity

The synchrotron emissivity as a function of synchrotron age is given by equation (1.10). Some simplifying assumptions are now made to solve for the proportionality constants κ_{new} and κ_{old} in terms of the flow variables. Since the two power-laws join at $\nu = \nu_{\text{br}}$ one can equate the two emissivity prescriptions in equation (1.10) at this break frequency and solve for κ_{old} in terms of κ_{new}:

$$\kappa_{\text{old}} = \kappa_{\text{new}} \, (B \, \sin\psi)^{(x+5)/2} \, \nu_{\text{br}}^{(x+5)/6} \, t_{\text{syn}}^{(x+5)/3}. \tag{2.26}$$

Using the power-law assumption, the total number of high-energy electrons in the 'new' portion of the spectrum may be obtained by integrating equation (1.7):

$$N_{\text{tot}} = \kappa_{\text{new}} \int_{E_1}^{E_2} E^{-x} dE = \frac{\kappa_{\text{new}}}{(x-1)} \left(\frac{1}{E_1^{(x-1)}} - \frac{1}{E_2^{(x-1)}} \right) = \frac{\kappa_{\text{new}}}{(x-1)} \left(\frac{1}{E_1^{(x-1)}} \right) \quad (2.27)$$

as $E_2 \to \infty$ and provided that $x > 1$ (~ 2.5 for most radio spectra). Solving for κ_{new} yields:

$$\kappa_{\text{new}} = (x - 1) \ N_{\text{tot}} \ E_1^{(x-1)}. \quad (2.28)$$

Following Clarke et al. (1989), it is assumed that $N_{\text{tot}} \propto \rho$ and $E_1 \propto e/\rho$. With these assumptions equation (2.28) may be re-written using $p = (\gamma - 1)e$:

$$\kappa_{\text{new}} \propto p^{(x-1)} \rho^{(2-x)} \ . \quad (2.29)$$

Substituting equation (2.29) into equation (2.26) yields:

$$\kappa_{\text{old}} \propto p^{(x-1)} \rho^{(2-x)} \ (B \ \sin\psi)^{(x+5)/2} \ \nu_{\text{br}}^{(x+5)/6} \ t_{\text{syn}}^{(x+5)/3}. \quad (2.30)$$

With κ_{new} and κ_{old} now solved equation (1.10) becomes:

$$i(\nu) \propto \begin{cases} p^{(x-1)} \rho^{(2-x)} \ (B \ \sin\psi)^{(x+1)/2} \ \nu^{-(x-1)/2} & \nu < \nu_{br} \\[2mm] p^{(x-1)} \rho^{(2-x)} \ (B \ \sin\psi)^{(x+1)/2} \ \nu_{\text{br}}^{(x+5)/6} \ \nu^{-(2x+1)/3} & \nu > \nu_{br} \ . \end{cases} \quad (2.31)$$

Equation (2.31) is the prescription for emissivity that is implemented for this work.

Chapter 3

Numerical Results

A set of 3-D numerical calculations were carried out using the ZEUS-3D code. A Mach 10, underdense ($\eta = \rho_j/\rho_a = 0.01$) jet with a trace toroidal magnetic field was launched into a uniform ambient medium. The jet orifice was located at the left boundary of the computational grid ($605 \times 325 \times 325$ zones) with the radius (r_j) resolved by 16 zones. A slight precession of the jet orifice was introduced to break the quadrantal symmetry of the calculation. The simulation was run until time $t = 7.0(r_j/c_a)$, where c_a is the ambient sound speed, at which point the bow shock reached the right edge of the grid. The simulation took 6 weeks to run on 16 2.5 GHz processors (ACE net's Fundy). Outflow boundary conditions were enforced everywhere except at the jet orifice and the left edge of the grid where reflecting boundary conditions were implemented. A resolution study was performed in order to ensure the numerical convergence of this calculation. The results of this study are shown in Fig. 3.1.

The synchrotron age distribution at the end of the high-resolution simulation is shown in detail in Fig. 3.2. Young inflowing fluid gradually ages along the length of the jet until strong shocks are encountered in the terminal region of the jet which re-energize the fluid. After passing through the shocks the fluid is left in the lobes where it continues to age. The ambient age is set to zero and does not contribute to
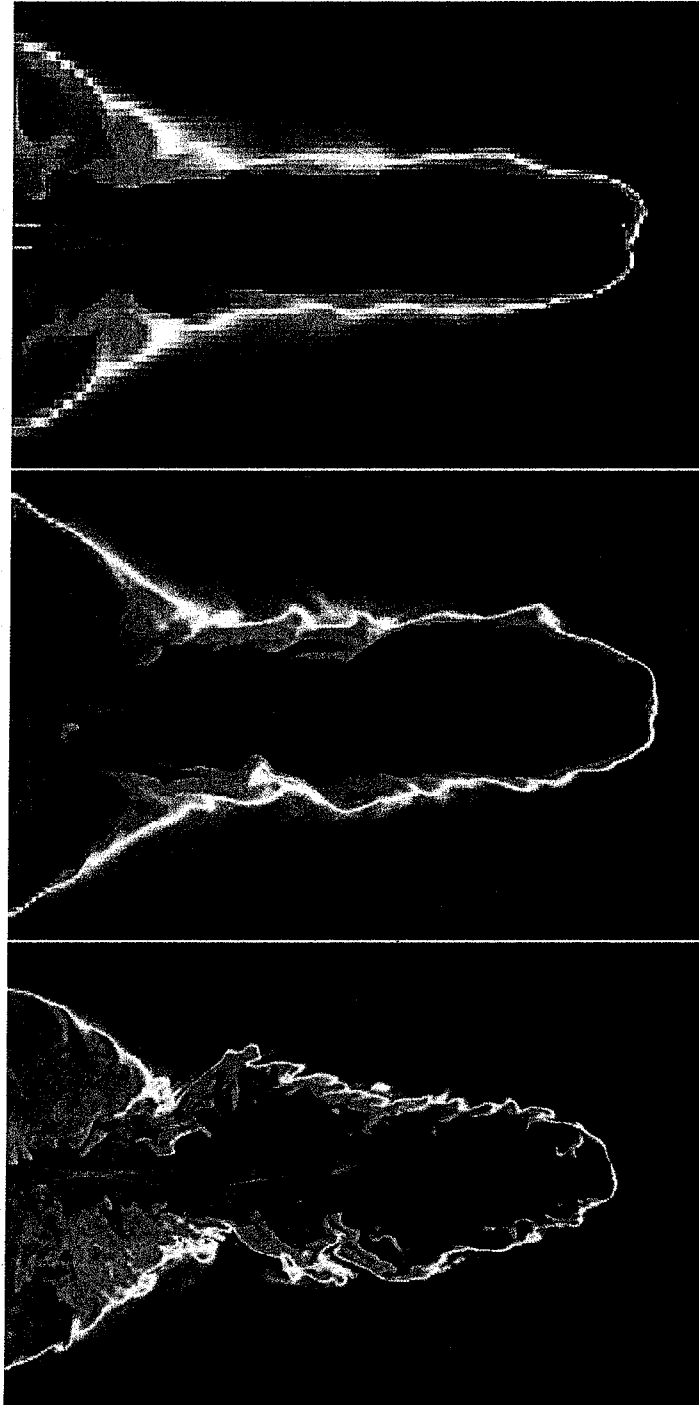
Figure 3.1: 2-D slices of the ρ distributions at the end of simulations with r_j resolved with 4, 8 and 16 zones (top-to-bottom). Blue/red corresponds to regions of under-dense/dense material. The similarity of these images (*e.g.* lengths, diameter of the lobe) indicates that the solutions are numerically convergent.

the synchrotron emission. By the end of the simulation, a filamentary magnetic field structure encompassed the jet (Fig. 3.3).

3.1   The Break Frequency (ν_{br}) and Scaling

Equation (1.13) shows that the break frequency is $\propto B^{-3} \, t_{\mathrm{syn}}^{-2}$. Accordingly, the magnetic field was combined with the synchrotron age to yield a three dimensional distribution of break frequency throughout the computational grid. A slice through this distribution is shown in Fig. 3.4.

The dimensionless break frequency needs to be scaled into physical units (Hz) for use in the emissivity relation given by equation (2.31). The synchrotron age and the magnetic field in physical units are obtained through the following scaling relations:

$$t_{\mathrm{syn}} = t_s \, \tilde{t}_{\mathrm{syn}} \tag{3.1}$$

$$B = B_s \, \tilde{B} \, , \tag{3.2}$$

where $\tilde{t}_{\mathrm{syn}}$ and $\tilde{B}$ are the dimensionless ZEUS-3D quantities and t_s and B_s are scale factors. There are two observational 'benchmarks' that need to be met to ensure the astrophysical plausibility of this synchrotron model. First, the source age must be $\sim 10^8$ yr which is set to the oldest synchrotron age on the grid. Therefore, solving equation (3.1) for t_s yields: $t_s = 10^8$ yr/$7.0 \sim 5 \times 10^{14}$ s. Second, the average break frequency should occur at around 5×10^9 Hz (~ 6 cm), as observed in most ERS. This is achieved by substituting equations (3.1) and (3.2) into equation (1.13), and

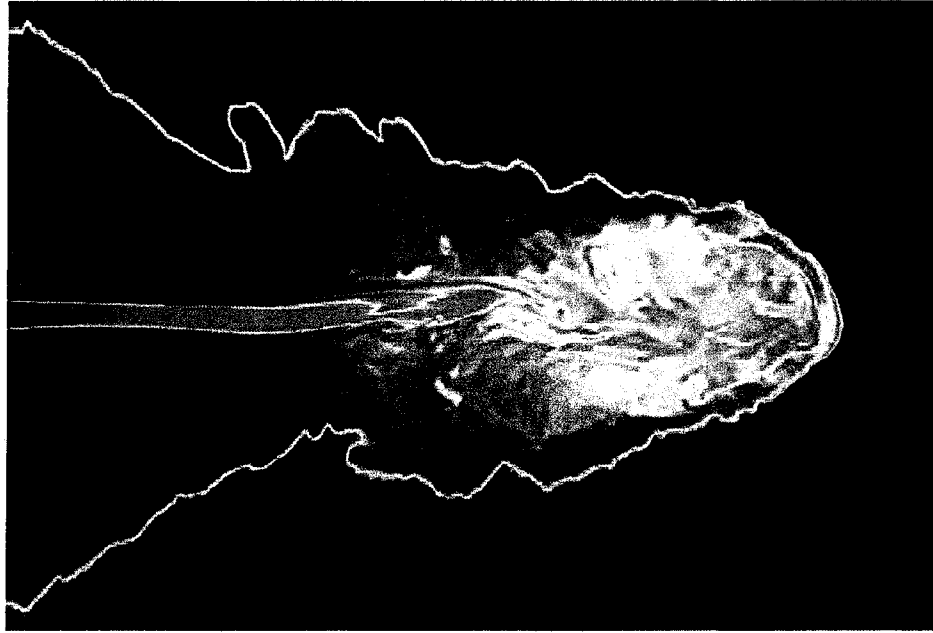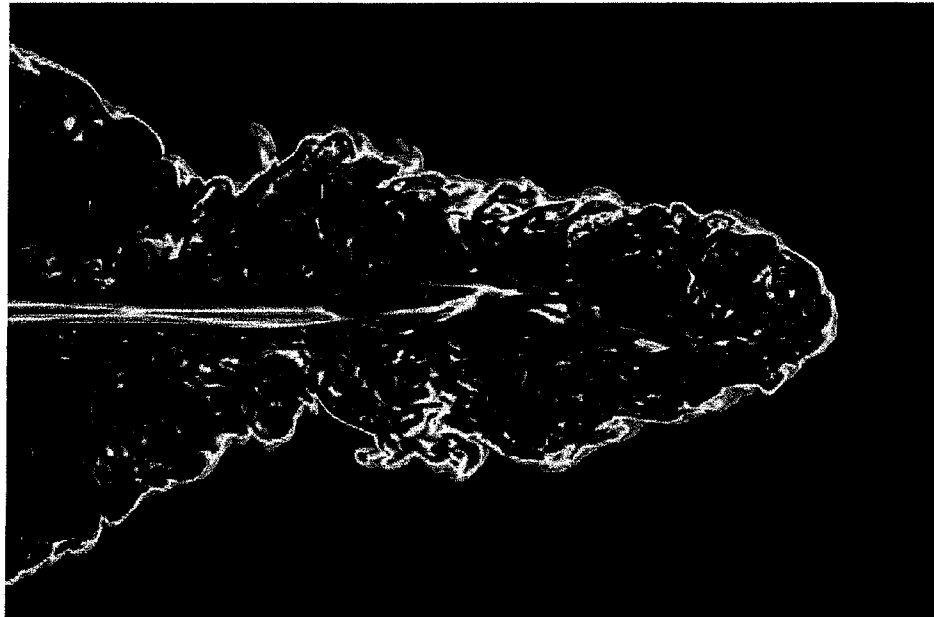Figure 3.2: A 2-D slice of the t_{syn} distribution. Blue/red corresponds to regions of young/old material.

Figure 3.3: A 2-D slice of the B distribution. Blue/red corresponds to regions of low/high magnetic field intensity.

using $\tilde{\nu}_{\mathrm{br}} = \tilde{B}^{-3} \, \tilde{t}_{\mathrm{syn}}^{-2}$ to obtain:

$$\nu_{br} = 4.1916 \times 10^{11} \, \tilde{\nu}_{\mathrm{br}} \, B_s^{-3} \, t_s^{-2} \, . \tag{3.3}$$

Inspection of the dimensionless break frequency distribution (*e.g.* Fig. 3.4) reveals that a transition from lobe dominated emission to jet dominated emission occurs over roughly a decade of frequency centred at $\tilde{\nu}_{br} \sim 10^{10}$ in dimensionless units. Thus, solving equation (3.3) for B_s yields $B_s \sim 2 \times 10^{-6} \, T$ at $\nu_{br} \sim 5 \times 10^9$ Hz. This scale factor, in addition to providing the desired spectral transition, results in an average magnetic field of $B \sim 10^{-9} \, T$ in the lobe, in agreement with the observational estimates presented in Table 1. With the break frequencies in place, synchrotron emissivities were computed in each zone using equation (2.31). A slice through this distribution is shown in Fig. 3.5.

3.2   Line-of-Sight Integrations

In order to make direct comparisons with observational measurements of synchrotron intensity from ERS, line-of-sight integrations of the emissivities computed with equation (2.31) are performed to obtain measures of the synchrotron intensity, $I(\nu)$:

$$I(\nu) = \sum_n i(\nu) \, \delta l_n \, , \tag{3.4}$$

where δl_n is the distance a given line of sight passes through the nth zone. The results of these line-of-sight integrations through the simulation are illustrated in Fig. 3.6
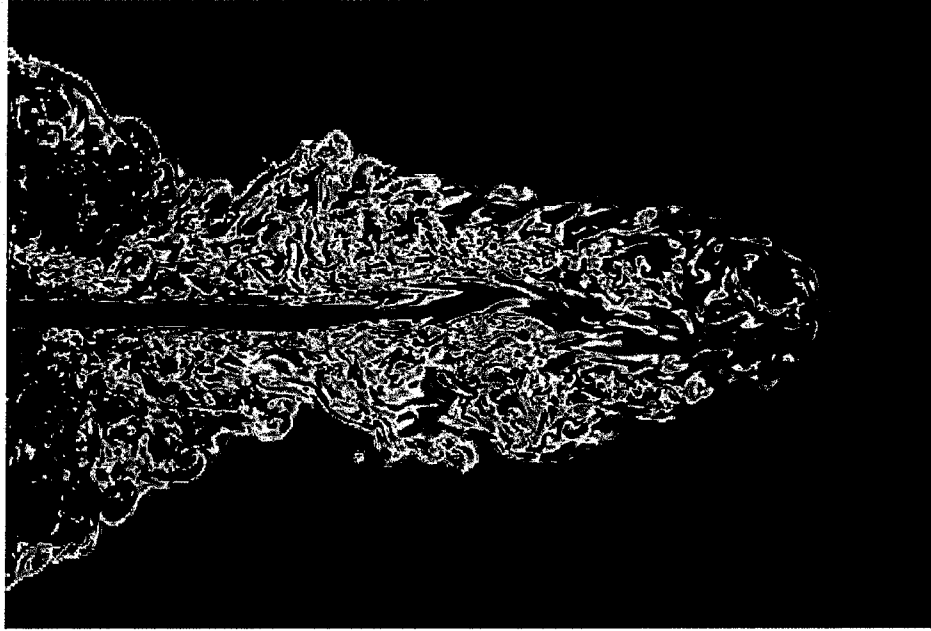
Figure 3.4: A 2-D slice of the ν_{br} distribution. Blue/red corresponds to regions of low/high break frequency.
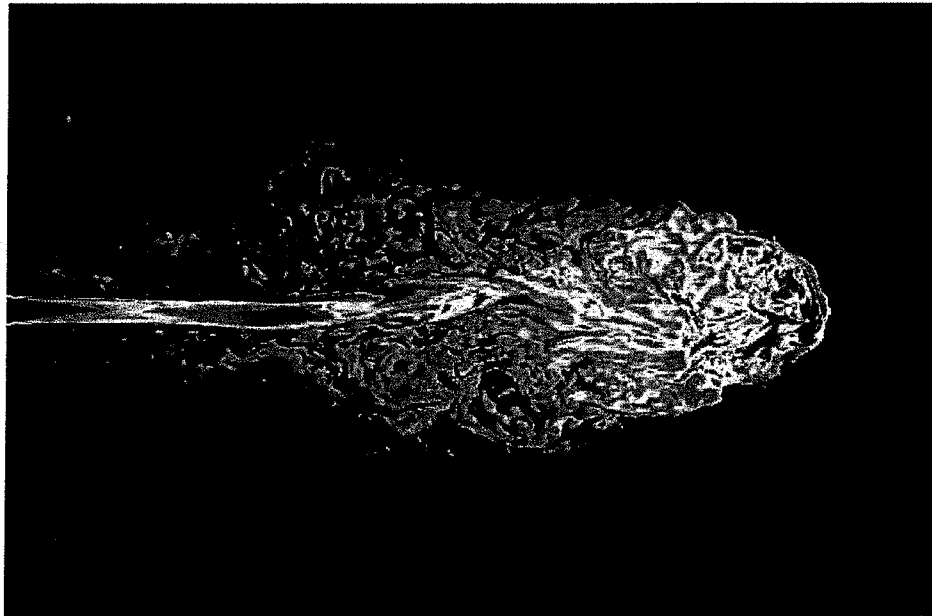

Figure 3.5: A 2-D slice of the i_ν distribution at 5.0×10^9 Hz. Blue/red corresponds to regions of low/high synchrotron emissivity.

which shows three separate observations at 20 cm, 6 cm and 2 cm respectively.

In contrast to Fig. 1.13 and similar to Fig. 1.14, the jet is clearly apparent in each of the three images. The transition from lobe dominated emission at 20 cm to jet dominated emission at 2 cm is evident in these synthetic images. In particular, a 'naked' jet, not encompassed by surrounding lobe emission, is revealed in the 2 cm observation whereas a 'bridge' of lobe emission, similar to the top panel of Fig. 1.11 is evident in the 20 cm observation. This intensity progression is made possible by the synchrotron age algorithm, since the contribution to the line-of-sight emission from the lobe decreases moving from the jet terminus back to the jet orifice. This decrease is a result of the lobe material aging as the jet moves forward leaving it behind (*e.g.* Fig. 3.2). This spectral progression is what was specifically omitted from the Clarke et al. (1989) model and is why the synchrotron intensity image illustrated in Fig. 1.13 shows a much more uniform lobe brightness (regardless of proximity to the hot spots or the jet orifice).

The frequency-dependent emission produced by this new synchrotron age algorithm represents a major advance in the ZEUS-3D code's ability to produce images that can be directly compared to real radio observations. In the spirit of making these comparisons, each image in Fig. 3.6 is further convolved with a Gaussian beam to mimic the resolution of real radio observations. The beam width ($r_b = 1.0$ in ZEUS-3D units) is chosen to be representative of the resolution of radio telescopes such as the National Radio Astronomy Observatory's Very Large Array (VLA). The results of these convolutions are shown in Fig. 3.7.
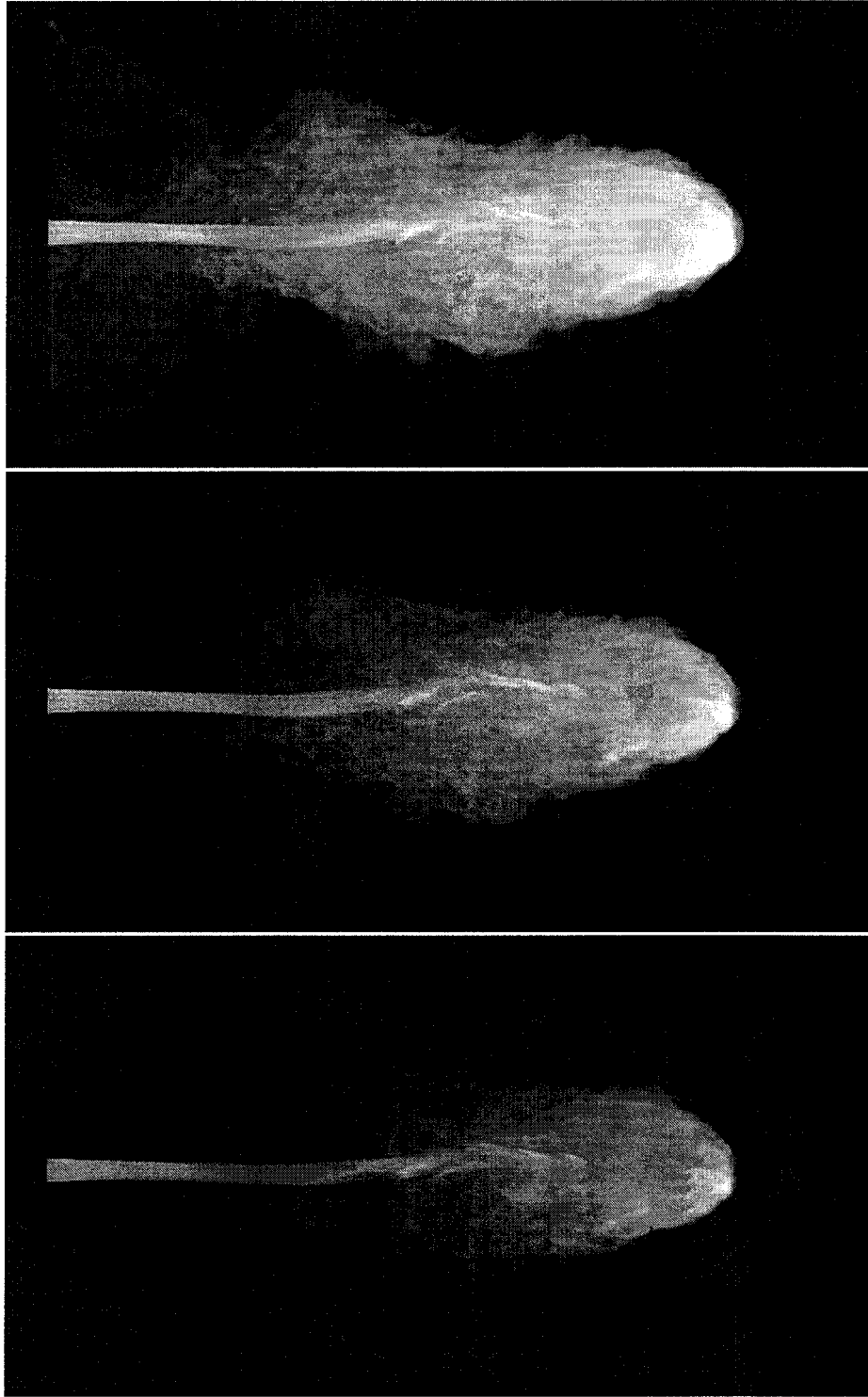
Figure 3.6: Radio images of the jet at 20 cm, 6 cm and 2 cm (top to bottom) using the new synchrotron age algorithm. White/black corresponds to regions of high/low synchrotron emission. The grey scale ranges over four orders of magnitude.
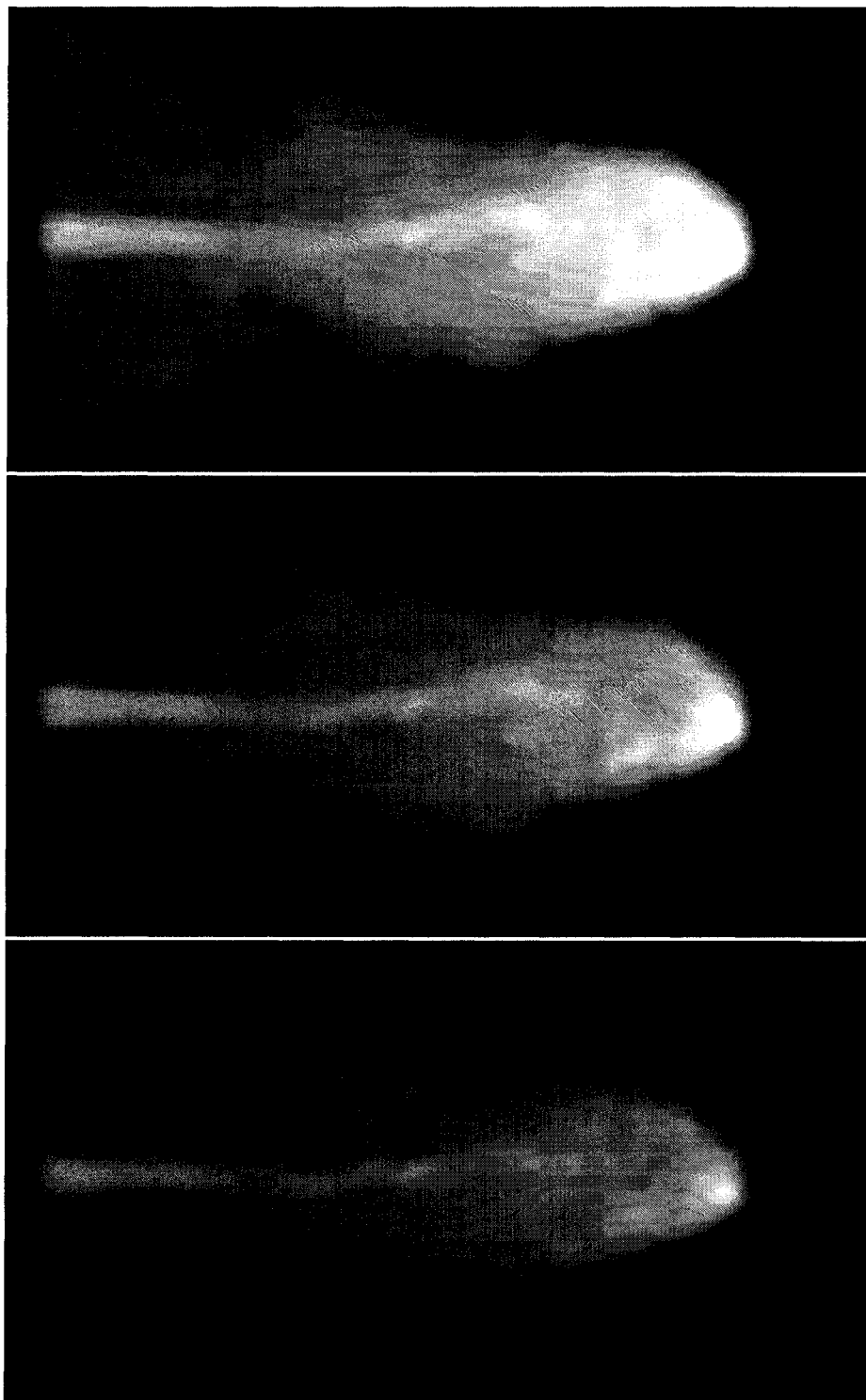
Figure 3.7: Radio images of the jet at 20 cm, 6 cm and 2 cm (top to bottom) convolved with a Gaussian beam of width $r_b = 1.0$. White/black corresponds to regions of high/low synchrotron emission. The grey scale ranges over four orders of magnitude.

3.3 Spectral Tomography

A tomography gallery (discussed in §1.3.1) is created from the convolved 20 cm and 6 cm observations shown in Fig. 3.7. An individual tomography intensity (I_t) is only included in the gallery if both measures of synchrotron intensity used to create I_t are above a set signal-to-noise ratio. In particular, I_t is included if both intensity measurements have a $S/N > 5$, where N is taken arbitrarily to be 10^{-20} in dimensionless units. Since the algorithm is designed to have the two limiting spectral slopes of $\alpha_{\text{new}} = (x-1)/2$ and $\alpha_{\text{old}} = (2x+1)/3$, the tomography spectral index (α_t) is tuned between these two values. For a power law index of $x \sim 2.5$, this yields a range of $0.75 < \alpha_t < 2.0$. The synthetic tomography gallery shown in Fig. 3.8 bears a resemblance to the Cygnus A gallery shown in Fig. 1.8.

Upon inspection of the gallery, one can see (as is the case with Cygnus A) that the hot spots disappear first, indicating that they have a flatter spectrum than the jet which does not fully drop out until the fourth frame. Several distinct spectral features within the lobe become apparent in the second frame of the gallery. These features are blended together in the total intensity images shown in Fig. 3.7, illustrating the tomography technique's power to isolate separate spectral components. The major difference between the synthetic gallery and the corresponding gallery of Cygnus A is that in Fig. 1.8 the jet first begins to disappear at around frame 8 ($\alpha_t \sim 1.2$) yielding a measure of the jet's spectral index. In contrast, the jet in the synthetic gallery first begins to disappear in frame 1 ($\alpha_t \sim 0.75$). Therefore, the simulated jet is radiatively 'younger' than the jet in Cygnus A. Rudnick & Katz-Stone (1996) point out that the
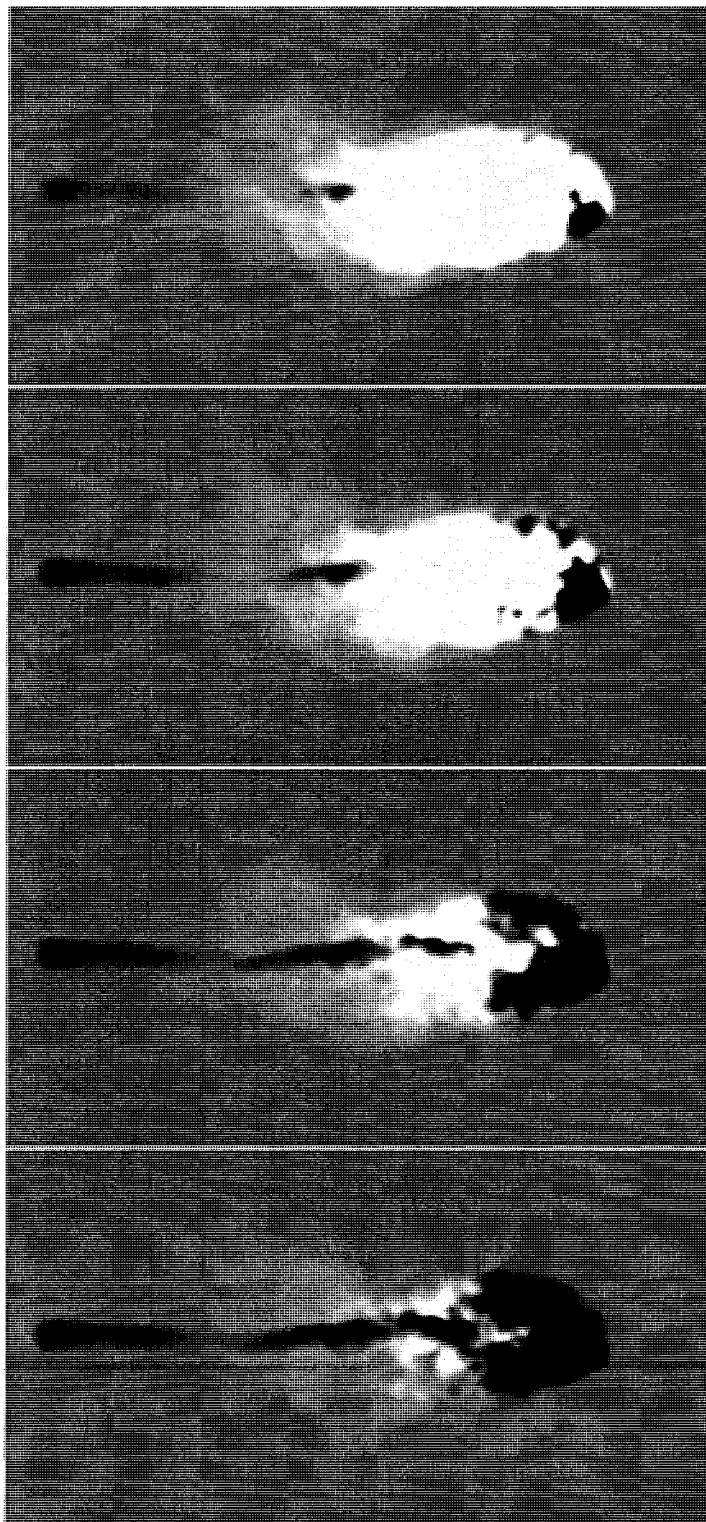
Figure 3.8: Synthetic spectral tomography gallery with $0.75 < \alpha_t < 2.0$ with a step size of 0.4 (top to bottom).

Cygnus A tomography sequence shows a channel of material surrounding the jet. A channel is perhaps evident in the third frame of the synthetic tomography sequence in Fig. 3.8 and is simply the contrast between the aged lobe and the young jet which has just disappeared from the image.

3.4 Colour-Colour Diagrams

Spectral index images [see equation (1.15)] are created from the convolved 2 cm, 6 cm and 20 cm radio observations shown in Fig. 3.7 and are illustrated in Figs. 3.9 and 3.10. Both the jet and the filamentary lobe are visible in each image. The main difference between these two spectral index images is that the α_{20}^6 image has generally flatter (whiter) spectral index values than the steeper (blacker) values of the α_6^2 image. This follows naturally, since at 20 cm there will be more regions where the spectral break frequency (ν_{br}) is larger than the observing frequency (ν_{obs}). This results in overall flatter observed spectral indices in contrast to the steeper 2 cm observations.

A colour-colour diagram (discussed in §1.3.2) was created from these two spectral index images and is shown in Fig. 3.11. Each point represents α_6^2 vs. α_{20}^6 at independent positions in the simulated source, where each position is separated from the next by a beam width (r_b). Similar to the tomography gallery, the colour-colour diagram is constructed from synchrotron intensity measurements with signal-to-noise ratios of $S/N > 5$.

The majority of points in this synthetic colour-colour diagram lie slightly below the power-law line indicating that spectral curvature, due to synchrotron losses, is
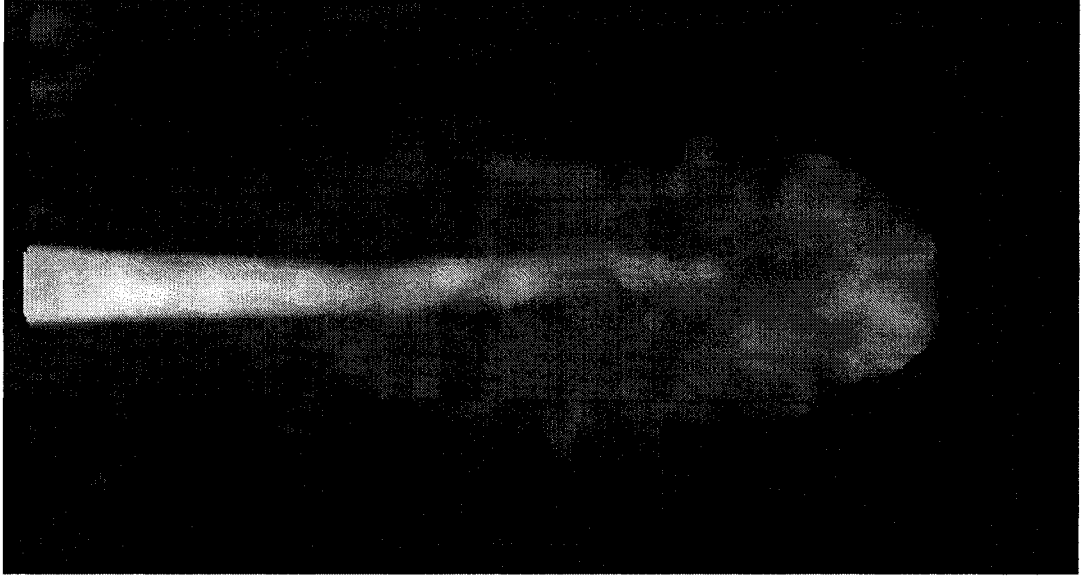
Figure 3.9: A spectral index image (α_6^2) created from the convolved 2 cm and 6 cm synthetic radio observations. The grey-scale ranges from -0.75 (white) to -2.0 (black).
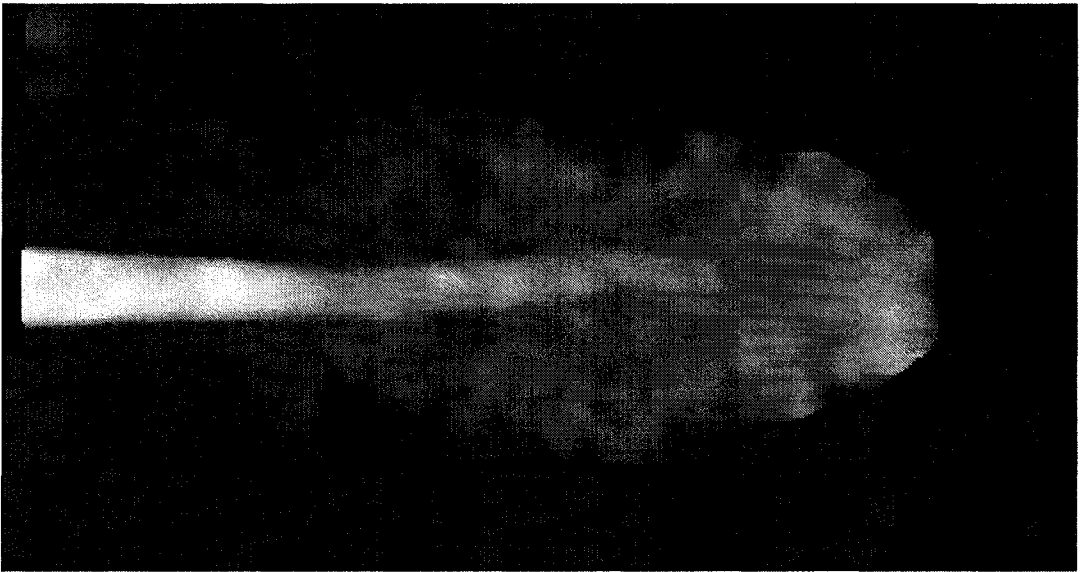

Figure 3.10: A spectral index image (α_{20}^6) created from the convolved 6 cm and 20 cm synthetic radio observations. The grey-scale ranges from -0.75 (white) to -2.0 (black).
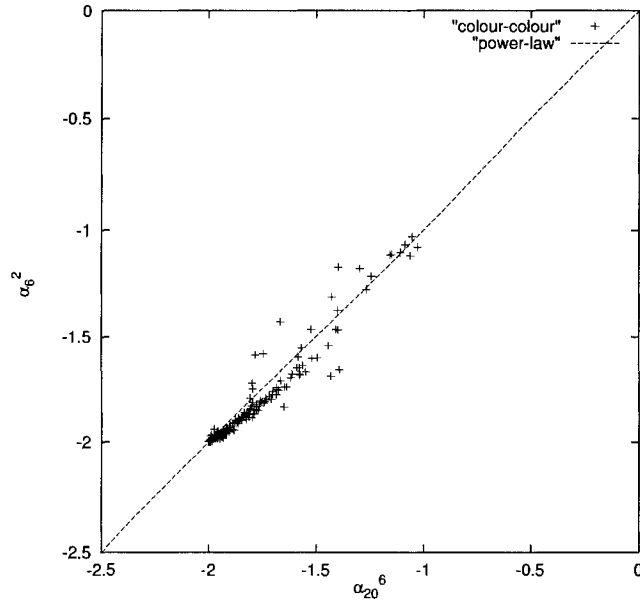
Figure 3.11: A colour-colour diagram created using the convolved α_6^2 and α_{20}^6 spectral index images. A strict single power-law locus is indicated with a dashed line.

present in the simulation. If there were no aging then all regions in the source would emit a young spectrum and $\alpha_6^2 = \alpha_{20}^6 = \alpha_{new} = -0.75$ for each position in the source. If on the other hand all regions in the source were radiatively "old" then $\alpha_6^2 = \alpha_{20}^6 = \alpha_{old} = -2.0$ for each position in the source. To illustrate this point, consider an idealized synchrotron spectrum (*e.g.* Fig. 1.6). If a spectral break does occur in an idealized spectrum (say at $\nu_{br} \sim 6$ cm) then α_{20}^6 will be a measure of the slope of the *young (flatter)* portion of the spectrum and α_6^2 will be a measure of the slope of the *old (steeper)* portion of the spectrum implying that $\alpha_6^2 < \alpha_{20}^6$. Therefore, as the spectra in the source are 'altered' by synchrotron losses, points move through the colour-colour plane and populate the region below the power-law line bounded by the two extrema index values α_{new} [see equation (1.9)] and α_{old} [see equation (1.11)]. This spectral progression is illustrated in Fig. 3.12.
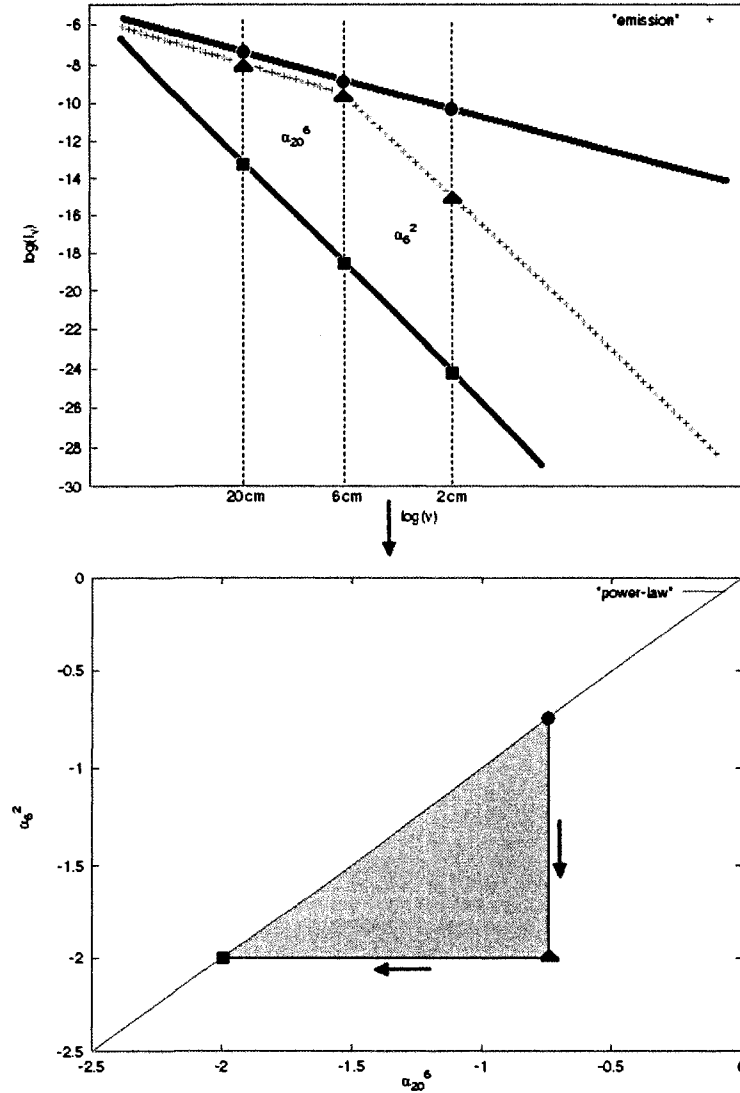
Figure 3.12: A simple model illustrating how spectra in the $\log(I_\nu)$ vs. $\log(\nu)$ plane translate into the colour-colour plane. The circles represent measurements of a 'young' spectrum with a uniform spectral index α_{new}. The triangles represent measurements of the same spectrum subjected to synchrotron losses (resulting in a spectral break at 6 cm). Finally, the squares represent measurements of the 'aged' spectrum with a uniform spectral index α_{old}. As the spectrum is altered over time, the spectral index points in the colour-colour plane move from the circle to the triangle and then to the square, mirroring the progression of the spectral break across the $\log(\nu)$ axis.

This 'aged' region in the colour-colour plane is precisely where the majority of points in the synthetic colour-colour diagram are found; however, it is evident that there are several outlying points that lie above the power-law line in Fig. 3.11. For these points $\alpha_6^2 > \alpha_{20}^6$ indicating that an inflection in the curvature of the spectrum has occurred. As will be discussed in the next section, this change in spectral curvature is a result of the superposition of two distinct spectral features, namely, the jet and the lobe, which lie along a given line-of-sight.

The synthetic colour-colour diagram shown in Fig. 3.11 is indicative of the dual power-law model incorporated into the simulation. In contrast, the colour-colour diagram for Cygnus A, shown in Fig. 1.9, indicates the underlying physics is more complex than a simple power-law model as it bears little resemblance to Fig. 3.11. In Cygnus A, the flatter emission regions seem to closely follow a power-law while the steeper emission regions deviate from it. For example, the α_{20}^6 spectral index measurements in Fig. 1.9 never exceed values of -2 even though the corresponding measures of α_6^2 reach values as low as -2.5. This indicates that on average the break frequency in Cygnus A must be $\nu_{\mathrm{br}} > 1.5 \times 10^9$ Hz. An attempt was made to duplicate the shape of the Cygnus A colour-colour diagram by plotting α_2^6 vs. α_{60}^{20}. The results of this colour-colour analysis are illustrated in Fig. 3.13 which shows further deviation of the points from the power-law line; however, the spectral 'bend' evident in Fig. 1.9 is not reproduced.

As well as not being able to produce the shape of the locus of points, the synthetic colour-colour diagrams cannot reproduce the range of spectral index values (-0.5 to -2.5) present in Fig. 1.9. This range of values points to a non-uniform distribution
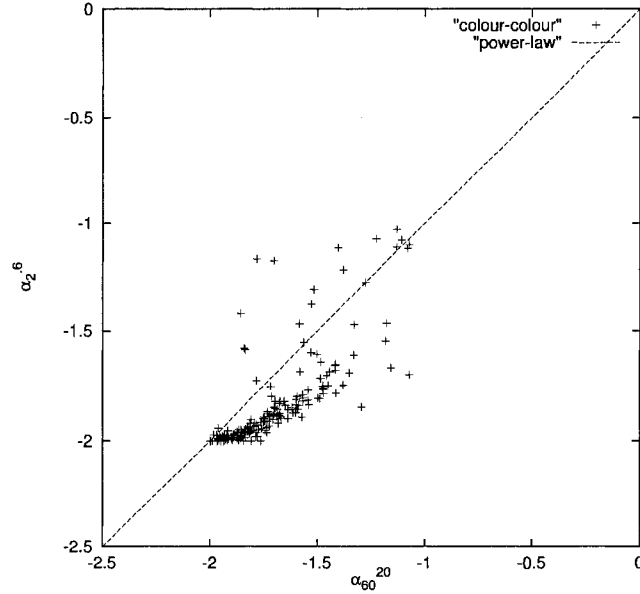
Figure 3.13: A colour-colour diagram created using convolved α_2^6 and α_{60}^{20} spectral index images. A strict single power-law locus is indicated with a dashed line.

of x, the underlying power-law index [see equation (1.7)], and perhaps indicates the existence of multiple high-energy electron populations contained within Cygnus A. As discussed in §1.3.2, there is no known analytic model that can produce this range of spectral curvature. Therefore, the single power-law index ($x = 2.5$) incorporated into this simulation is unable to reproduce the full range of spectral curvature that is observed within Cygnus A.

3.5 Physical Pair Images

Finally, an attempt is made to create the three physical pair images discussed in §1.3.3 from the simulated synchrotron emission. First, a distinction must be made between the break frequency in an individual zone on the MHD grid $[\nu_{\mathrm{br}}(i, j, k)]$

and the 'observed' break frequency (ν_{br}^{obs}) in a spectrum created from line-of-sight integrations of synchrotron emissivity through the source. The former is determined directly from the local magnetic field strength and the synchrotron age, while the latter is a complicated function of all the contributing zones along each line-of-sight.

To illustrate the effects of line-of-sight variations on the observed break frequency consider Fig. 3.14 and Fig. 3.15. Fig. 3.14 shows the dual power-law spectrum of an individual zone in the MHD grid with a well defined spectral break. Fig. 3.15 depicts the superposition of two power-law spectra from two different zones with different break frequencies. This superposition results in a curved portion in the spectrum that deviates from a strict power-law. These deviations are evident in some of the observed spectra obtained from the simulated emission. Fig. 3.16 shows the observed spectrum along a line-of-sight that passes through both the jet and the lobe.

The tell-tale cusp in Fig. 3.15 is evident in the spectrum of Fig. 3.16 suggesting that there are two dominant sources of emission with different spectral break frequencies along this particular line-of-sight, namely, the jet and the lobe. In contrast, Fig. 3.17 shows the observed spectrum along a line-of-sight that excludes the jet. This spectrum is devoid of the large cusps present in previous spectrum. When the contributions from jet are subtracted from the line-of-sight integrations by using the fluid velocity as a filter, the spectrum shown in Fig. 3.16 resembles that shown in Fig. 3.17.

Evidently, numerous points along a line-of-sight with distinct spectral breaks can result in a complicated spectrum full of bumps, wiggles, *etc.* (hinted at by our colour-colour analysis) that would not normally be associated with a power-law spectrum.
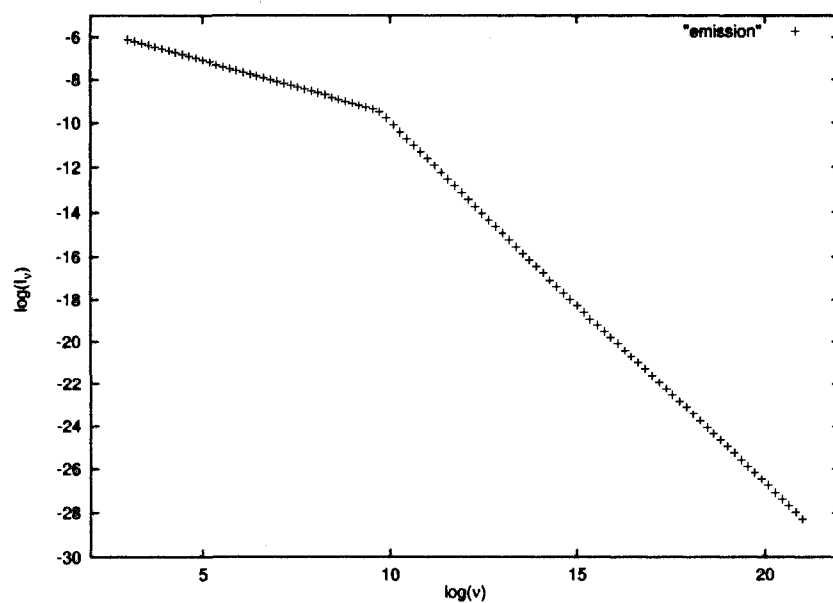
Figure 3.14: The emissivity spectrum of an individual zone in the computational grid.
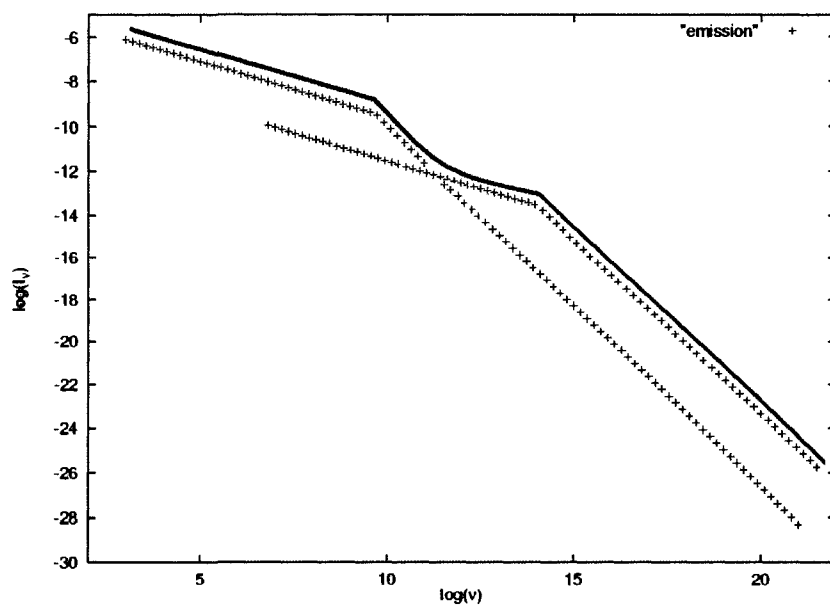

Figure 3.15: Model superposition of two power-law components that lie along a given line-of-sight.
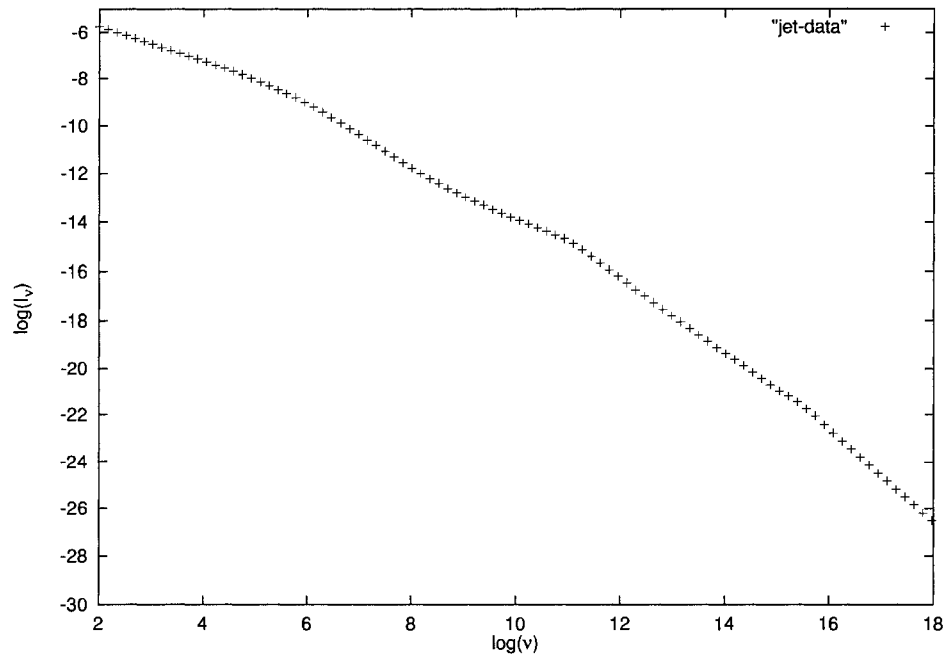
Figure 3.16: Synchrotron spectrum for a position in the jet region of the model ERS.
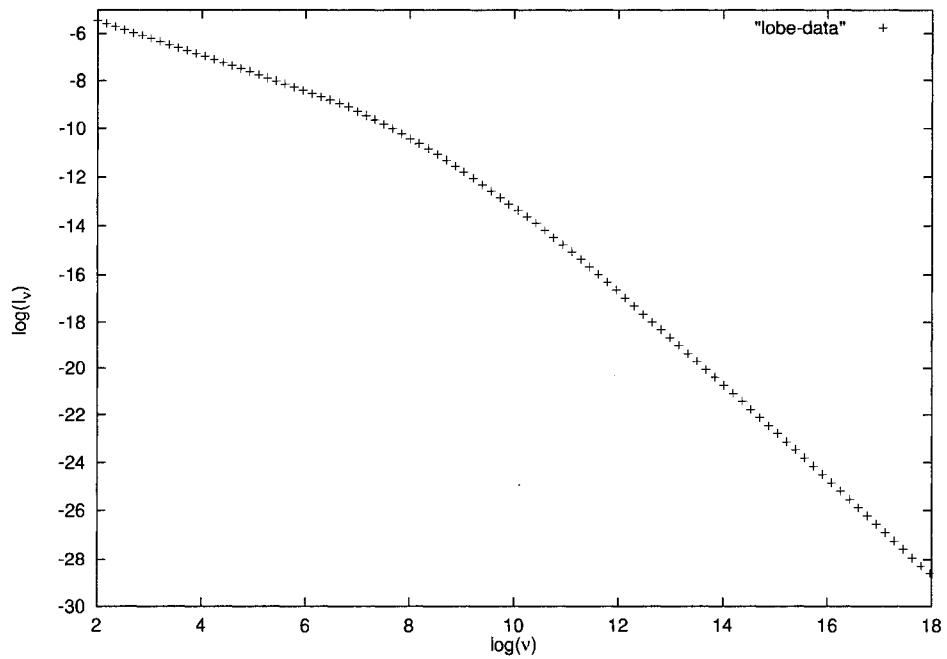

Figure 3.17: Synchrotron spectrum for a position in the lobe region of the model ERS.

However, two features from the spectra of an individual zone do survive the spectral superposition, namely, the low and high frequency extrema. The low and high frequency portions of the observed spectrum represent the *young* and *old* portions of the original underlying dual power-laws. It is these spectral extrema that are used, as shown below, to define an 'overall' observed break frequency (ν_{br}^{obs}) and thus the reference frequency required to construct the physical pair images discussed in §1.3.3.

In order to determine ν_{br}^{obs} at each position on the radio plane, the extrema of the grid break frequency [$\nu_{br}(i,j,k)$] distribution (ν_{br}^{min} and ν_{br}^{max}) are used. Knowing these limiting frequencies allows one to make a determination of ν_{br}^{obs} by using a limited number of n multi-frequency observations which 'bracket' the break frequency extrema. If the frequencies of the initial (ν_i) and final (ν_f) observations are set such that: $\nu_i < \nu_{br}^{min}$ and $\nu_f > \nu_{br}^{max}$, then one is guaranteed that the slopes of the various observed spectra at each position on the radio plane at these two limiting frequencies will be α_{new} (~ 0.75) and α_{old} (~ 2.0) respectively. In order to illustrate this point, the spectral index variations of the jet and lobe spectra (Fig. 3.16 and Fig. 3.17) discussed above are shown in Fig. 3.18 and Fig. 3.19 respectively. These two figures highlight the spectral structure contained along each line-of-sight and also illustrate the limiting spectral behavior, namely, the values of α_{new} and α_{old} at the ends of each spectrum.

Knowing these two limiting slopes and the frequencies at which they occur enables one to solve for the observed break frequency (ν_{br}^{obs}), and thus the reference frequency (ν_{ref}), directly. In particular, ν_{br}^{obs} is determined at each position using a simple interpolation scheme illustrated in Fig. 3.20.
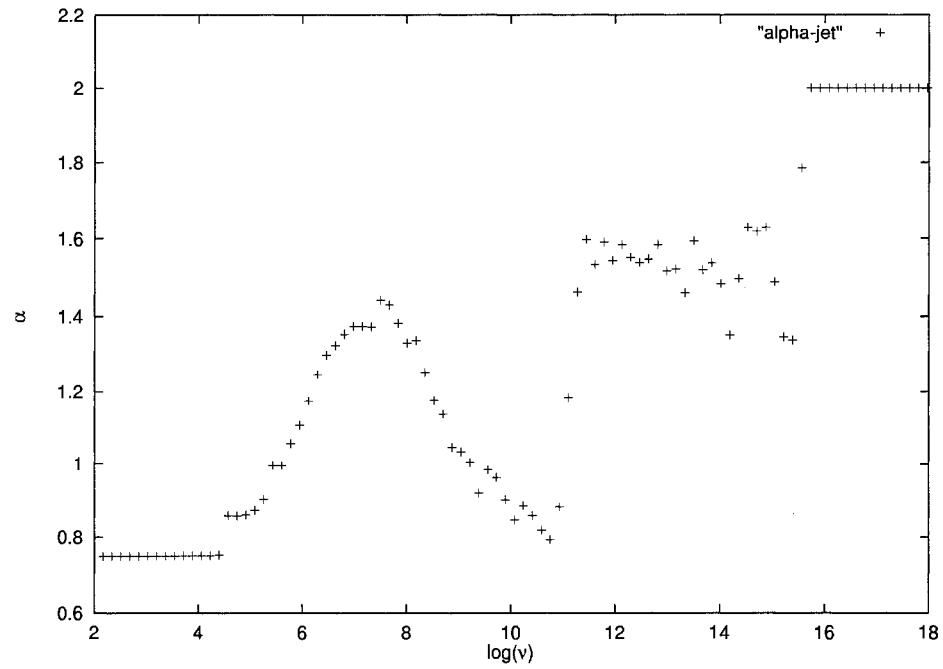
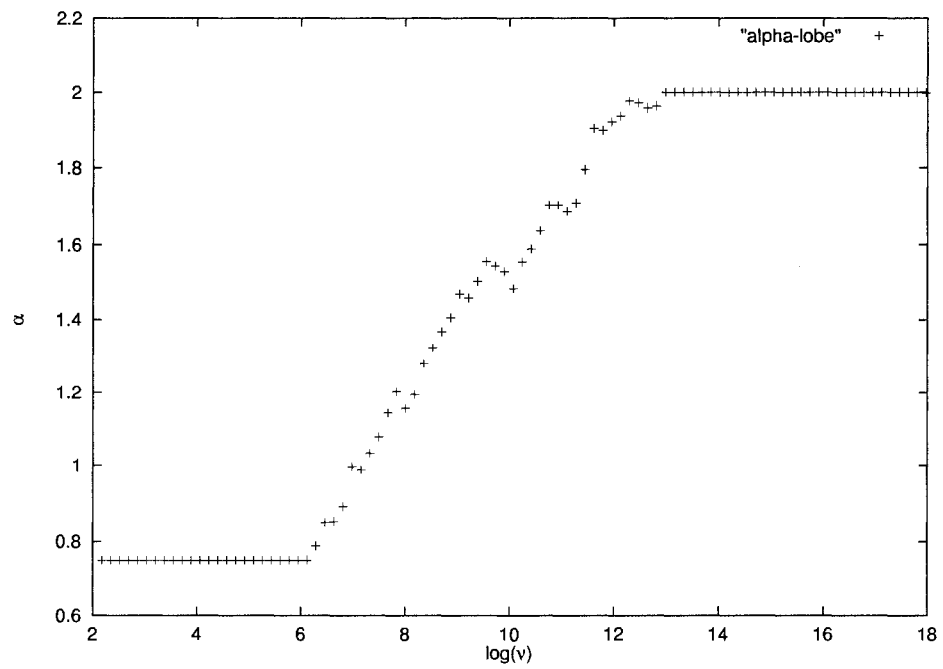Figure 3.18: Spectral index variations for the jet spectrum shown in Fig. 3.16.

Figure 3.19: Spectral index variations for the lobe spectrum shown in Fig. 3.17.
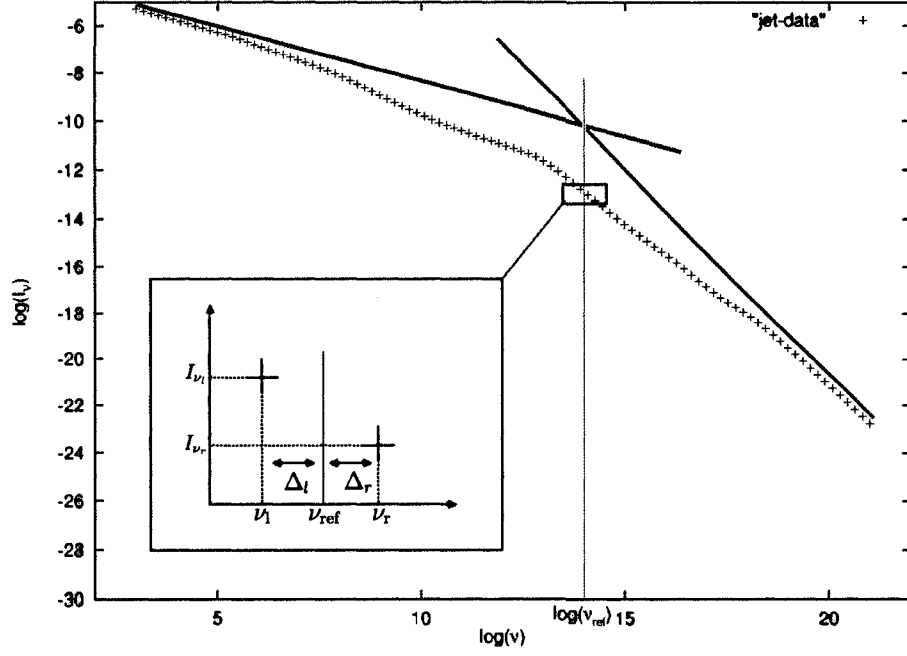
Figure 3.20: Linear interpolation procedure for determining ν_{ref} and $I(\nu_{ref}, \vec{r})$. ν_{ref} is located at the intersection of the two lines given by equations (3.5) and (3.6) for each position in the source. Then (shown in inset) $I(\nu_{ref}, \vec{r})$ is determined via a linear interpolation between the intensities observed at the two frequencies (ν_l and ν_r) that bracket ν_{ref}.

The two limiting slopes of each observed spectrum define two lines that intersect at ν_{br}^{obs}:

$$\log[\, I_{\nu_{new}}(\vec{r})\,] \;=\; \alpha_{new}\,\log(\nu_{new}) + b_{new}(\vec{r}) \tag{3.5}$$

$$\log[\, I_{\nu_{old}}(\vec{r})\,] \;=\; \alpha_{old}\,\log(\nu_{old}) + b_{old}(\vec{r})\,, \tag{3.6}$$

where $b_{new}(\vec{r})$ and $b_{old}(\vec{r})$ are, respectively, the intercepts of the two limiting spectra. By equating $\log[\, I_{\nu_{new}}(\vec{r})\,]$ and $\log[\, I_{\nu_{old}}(\vec{r})\,]$ (an equality which occurs at the spectral break) and using the fact that at the break $\nu_{new} = \nu_{old} = \nu_{br} \equiv \nu_{ref}$ one obtains:

$$\nu_{ref} = 10^{\left(\frac{b_{old}(\vec{r}) - b_{new}(\vec{r})}{\alpha_{new} - \alpha_{old}}\right)}. \tag{3.7}$$

The intercepts $b_{\text{new}}(\vec{r})$ and $b_{\text{old}}(\vec{r})$ vary with position and are computed, via equations (3.5) and (3.6), at the two extrema frequencies (ν_i and ν_f) for each position in the source.

With the reference frequencies determined by equation (3.7), the task remains to compute $I(\nu_{\text{ref}}, \vec{r})$. Instead of performing individual line-of-sight integrations for each position's ν_{ref}, which would require many more multi-frequency observations than would be realistically available to a radio astronomer, a simple linear interpolation is carried out to determine the reference intensity $I(\nu_{\text{ref}}, \vec{r})$ from the observed spectrum at each position on the radio plane:

$$I(\nu_{\text{ref}}, \vec{r}) = \frac{I_{\nu_l}(\vec{r})\Delta_r + I_{\nu_r}(\vec{r})\Delta_l}{\Delta_r + \Delta_l} , \qquad (3.8)$$

where $\Delta_l = |\nu_{\text{ref}} - \nu_l|$ and $\Delta_r = |\nu_{\text{ref}} - \nu_r|$. $I_{\nu_l}(\vec{r})$ and $I_{\nu_r}(\vec{r})$ are the intensities measured at the left and right frequencies that most closely bracket the reference frequency ($\nu_l < \nu_{\text{ref}} < \nu_r$) of the n set observational frequencies (Fig. 3.20). The top panels of Fig. 3.21 and Fig. 3.22 show images of $I(\nu_{\text{ref}}, \vec{r})$ which Katz-Stone & Rudnick (1994) claim are measures of $B(\vec{r})$ $N_T(\vec{r})$. The middle panels of Fig. 3.21 and Fig. 3.22 show images of ν_{ref} which are supposedly measures of $E_0^2(\vec{r})$ $B(\vec{r})$. Finally, to obtain an image of $N_T(\vec{r})/E_0^2(\vec{r})$, one simply takes the ratio $I(\nu_{\text{ref}}, \vec{r})/\nu_{\text{ref}}$ as outlined in §1.3.3. This is shown in the final panels of Fig. 3.21 and Fig. 3.22. The absence/prominence of the jet is the main feature in each image.

Upon comparison with Fig. 1.12 it is evident that the synthetic pair images bear little resemblance to the corresponding images created from observations of Cygnus A.
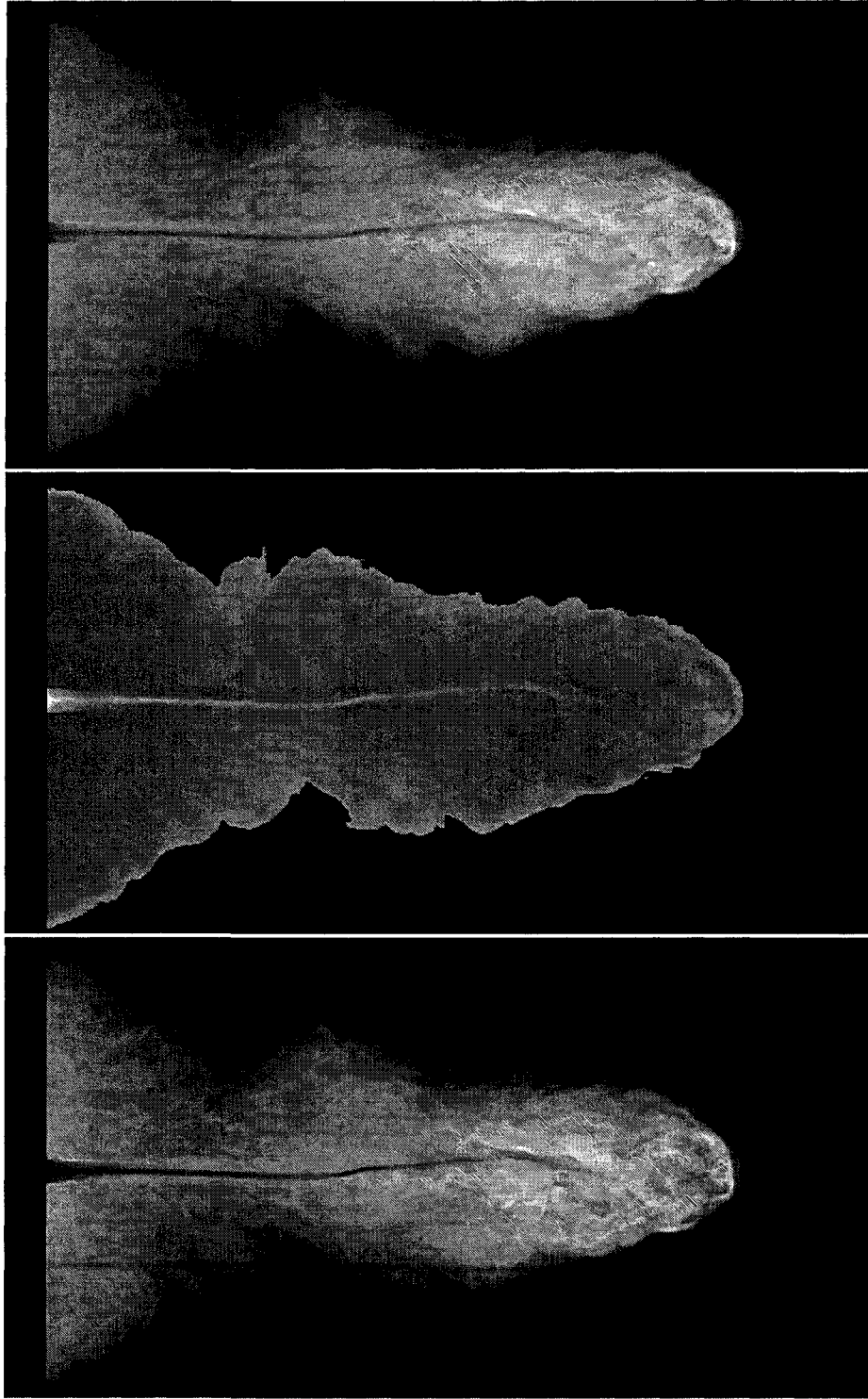
Figure 3.21: Katz-Stone physical pair images: grey scale images of $I(\nu_{\mathrm{ref}}, \vec{r})$, ν_{ref} and $I(\nu_{\mathrm{ref}}, \vec{r})/\nu_{\mathrm{ref}}$ (top to bottom).
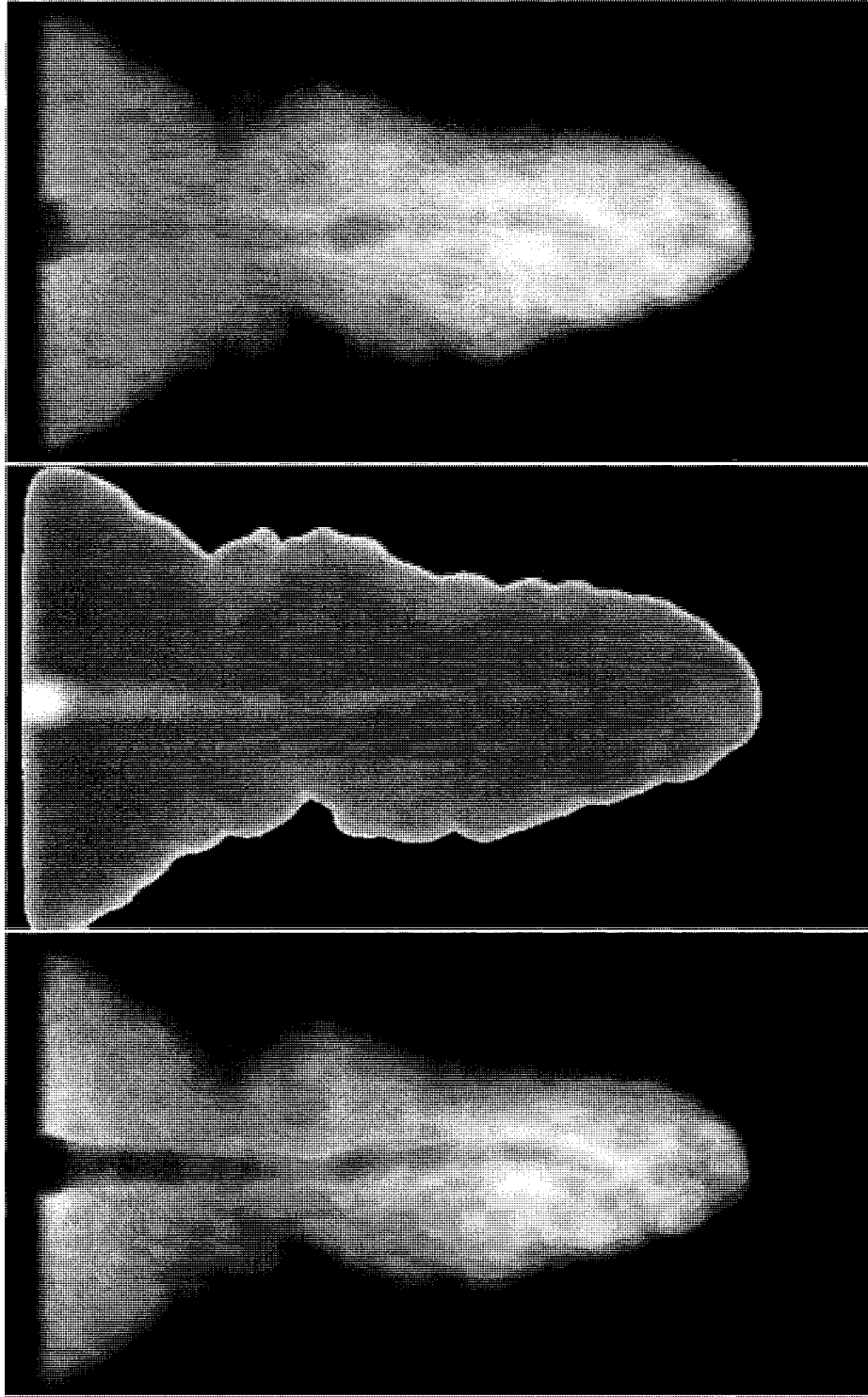
Figure 3.22: Katz-Stone physical pair images: grey scale images of $I(\nu_{\mathrm{ref}}, \vec{r})$, ν_{ref} and $I(\nu_{\mathrm{ref}}, \vec{r})/\nu_{\mathrm{ref}}$ (top to bottom) created with intensities convolved with a Gaussian beam of width $r_b = 1.0$.

In particular, the $I(\nu_{\text{ref}}, \vec{r})$ and $I(\nu_{\text{ref}}, \vec{r})/\nu_{\text{ref}}$ pair images exhibit emission surrounding the jet. The second pair image (ν_{ref}) is similar to the equivalent image for Cygnus A in that in both these images the jet is visible. However, in the Cygnus A image the hot spots are clearly visible as well, while they are absent in the synthetic image.

While there is no particular reason why the simulated pair images should bear a qualitative similarity to the corresponding images of Cygnus A (no attempt has been made to reproduce the specific physical conditions there), the claim made by Katz-Stone & Rudnick (1994) that images of $I(\nu_{\text{ref}}, \vec{r})$, ν_{ref} and $I(\nu_{\text{ref}}, \vec{r})/\nu_{\text{ref}}$ are measures of the physical variable pairs: $B(\vec{r})$ $N_T(\vec{r})$, $E_0^2(\vec{r})$ $B(\vec{r})$ and $N_T(\vec{r})/E_0^2(\vec{r})$ can still be tested. With the assumptions made in §2.4, namely, $N_T \propto \rho$ and $E_0 \propto e/\rho$, line-of-sight integrations of $B(\vec{r})$ $N_T(\vec{r})$, $E_0^2(\vec{r})$ $B(\vec{r})$ and $N_T(\vec{r})/E_0^2(\vec{r})$ are carried out. These integrations can then be compared directly to the $I(\nu_{\text{ref}}, \vec{r})$, ν_{ref} and $I(\nu_{\text{ref}}, \vec{r})/\nu_{\text{ref}}$ images. If the Katz-Stone method is correct and the assumptions about the line-of-sight effects are justified, similarities between these two sets of images should be apparent. Fig. 3.23 and Fig. 3.24 show the direct integrations of the ZEUS-3D variables and it is immediately apparent that they bear little resemblance to Fig. 3.21 and Fig. 3.22. The jet is not visible at all in contrast to the visible jet structure produced by the Katz-Stone method. Instead, these new images highlight the filamentary structure in the lobes. At the very least, this result indicates that the line-of-sight variations of $E(\vec{r})$ and $B(\vec{r})$ *cannot* be neglected.
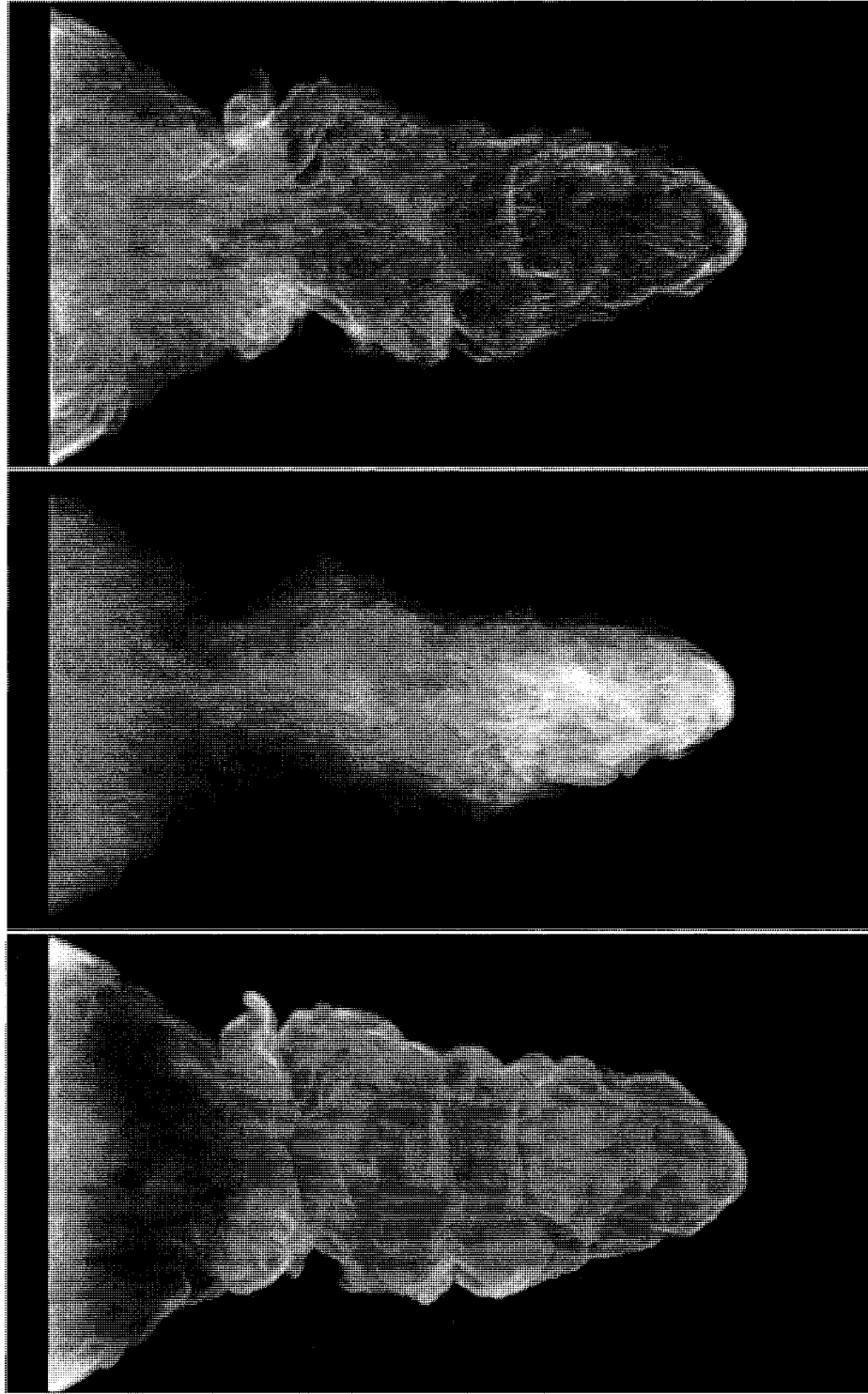
Figure 3.23: Line-of-sight integrations of the ZEUS-3D variable pairs: $B\rho$, $(e/\rho)^2 B$ and ρ^3/e^2 (top to bottom).
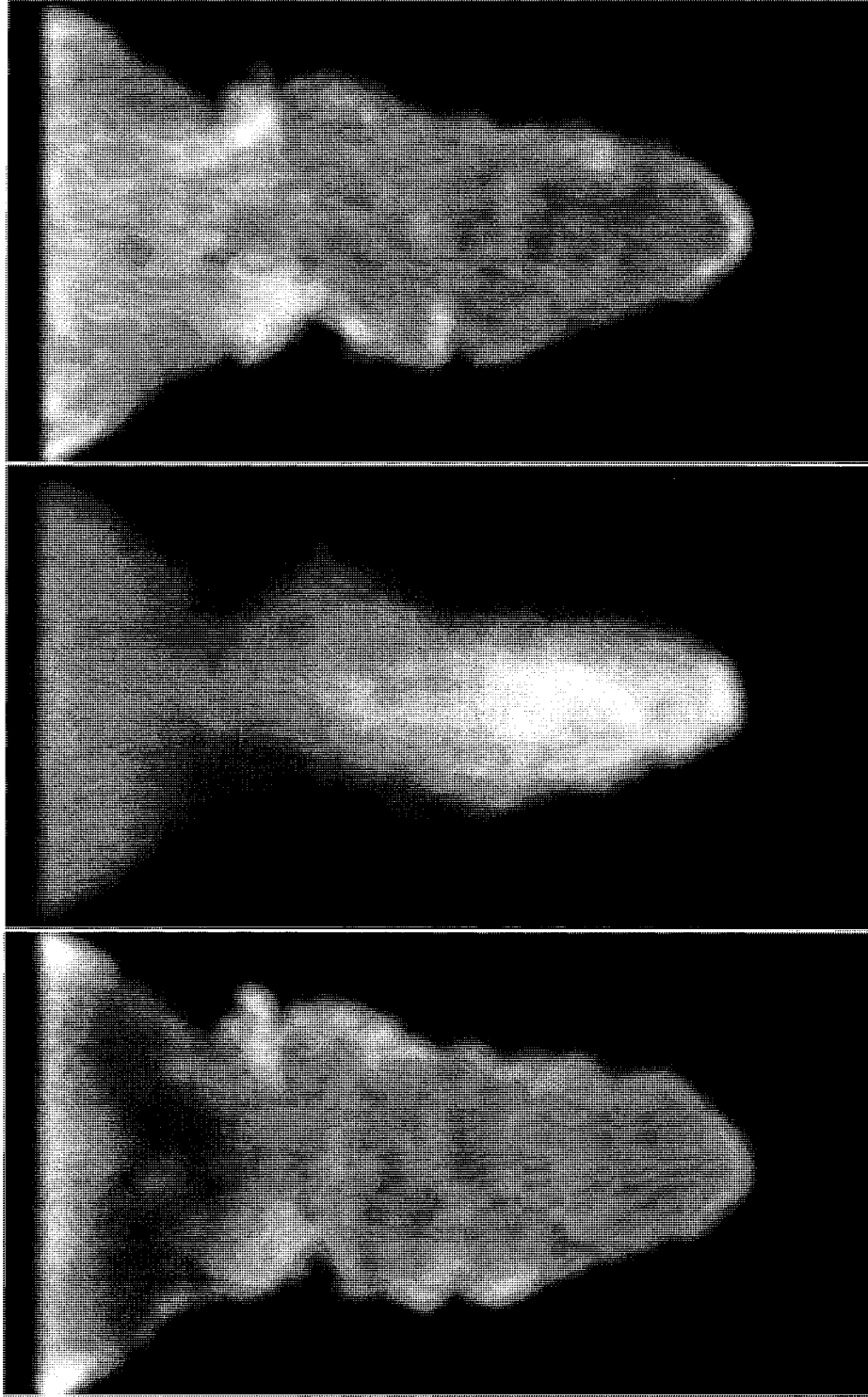
Figure 3.24: Line-of-sight integrations of the ZEUS-3D variable pairs: $B\rho$, $(e/\rho)^2 B$ and ρ^3/e^2 (top to bottom) convolved with a Gaussian beam of width $r_b = 1.0$.

3.6 Discussion

With the addition of the single 3-D scalar, t_{syn}, the ZEUS-3D code is able to produce a full suite of synthetic multi-frequency radio observations. The algorithm used to produce these observations is different from the model implemented by Tregillis, Jones & Ryu (2001) which required the addition of a minimum of eight 3-D scalars (the momentum bins). This new algorithm's simultaneous strength and weakness comes from its simplicity. Unlike the Tregillis, Jones & Ryu (2001) model, this algorithm does not model self-consistently the momentum sub-structure of a population of high-energy electrons embedded in an MHD flow. Instead, as discussed in §2.4, it is assumed that the power-law model put forward by Kardashev is sufficient to model the synchrotron emissivity of each zone. Therefore, the model is strictly semi-empirical. This being said, it is evident from the synthetic images presented in this chapter that, despite this drawback, the algorithm is able to re-produce the global synchrotron properties observed from ERS.

One major short-coming of this algorithm is the lack of a radiative history for each individual element of fluid. While the synchrotron age of the fluid has been tracked, this age is simply the time since injection and is only modified by shock re-acceleration. The radiative history of each element of fluid is not tracked. Consider a situation in which two identically aged elements of fluid pass through two distinct regions of magnetic field, one high and the other low, in the absence of any shocks. If the two elements of fluid were observed while they were contained within these two distinct regions one would measure two distinct break frequencies [see eqn (1.13)].

If these two elements of fluid then converged downstream into a region of uniform magnetic field, their break frequencies would be identical despite the fact that one element experienced greater synchrotron losses in the high field region upstream. This lack of radiative history illustrates a crucial aspect of the synchrotron mechanism that is not currently accounted for by this model.

From an observational standpoint, this synchrotron model has been able to reproduce some but not all of the observational benchmarks of an ERS as illustrated in the various comparisons between the synthetic images and real radio observations made in this chapter. In particular, the radio images shown in Fig. 3.6 and Fig. 3.7 capture both the basic morphology observed in ERS and also the transition from lobe-dominated emission to jet-dominated emission over the same decade of frequency as is observed in real radio sources. It should be stated that the scaling factors necessary to produce this radio emission are all well within the realm of astrophysical plausibility as discussed in §3.1. In addition to this similarity, the synthetic tomography gallery shown in Fig. 3.8 is similar to the gallery for Cygnus A shown in Fig. 1.8. This similarity seems to indicate that despite the short-comings of the model, the overall algorithm is still correctly simulating some of the physical mechanisms that produce the radio emission from these types of jets.

The colour-colour analysis reveals that the model is unable to account fully for the observed spectral curvature in Cygnus A. There is no known analytic model, however, that can reproduce the observed curvature. Therefore it remains to be determined what modifications to the existing algorithm are required to allow this synchrotron model to accurately reproduce the spectral curvature found in a source like CygnusA.

The final and perhaps most important comparison made was between the synthetic and observed parameter pair images. Having computed a full 3-D MHD jet simulation it is possible to make direct comparisons between the pair images that are generated from the 2-D multi-frequency observations shown in Fig. 3.6 and Fig. 3.7 and the line-of-sight integrations of the variable pairs from the 3-D data set. At the very minimum, Figs. 3.21-24 illustrate that line-of-sight variations cannot be neglected in these sources. The differences illustrated in these figures call into question the ability of the Katz-Stone technique to accurately image the variations of the three physical parameters, namely, the number density, electron energy and magnetic field, across a radio source.

Appendix A

The Scalar χ

The scalar χ introduced in §2.1 and defined as $\chi \equiv \hat{B} \cdot (\hat{B} \cdot \nabla)\vec{v}$ is expanded in Cartesian coordinates and evaluated directly. Thus,

$$
\begin{aligned}
\chi \;=\;\; & \hat{B}_x \left(\hat{B}_x \partial_x v_x + \hat{B}_y \partial_x v_y + \hat{B}_z \partial_x v_z \right) \\
+\;\; & \hat{B}_y \left(\hat{B}_x \partial_y v_x + \hat{B}_y \partial_y v_y + \hat{B}_z \partial_y v_z \right) \\
+\;\; & \hat{B}_z \left(\hat{B}_x \partial_z v_x + \hat{B}_y \partial_z v_y + \hat{B}_z \partial_z v_z \right) .
\end{aligned}
$$

The unit vectors $\hat{B}_x$, $\hat{B}_y$ and $\hat{B}_z$ are constructed from averages of $\vec{B}_x$, $\vec{B}_y$ and $\vec{B}_z$ to the zone centres respectively. The velocity derivatives are evaluated using van Leer (1974) differences, namely

$$
\partial_x v_n(i) = \begin{cases} 2 \left\{ \dfrac{\epsilon}{v_n(i+1)-v_n(i-1)} \right\} \dfrac{1}{\delta x(i)} & \epsilon > 0 \\[2ex] 0 & \epsilon < 0 \, , \end{cases} \tag{A.1}
$$

where $\epsilon = [v_n(i+1) - v_n(i)][v_n(i) - v_n(i-1)]$ and $n = x, y, z$. This differencing technique has the desirable property that $v_n(i)+\delta v_n(i)$ lies between $v_n(i)$ and $v_n(i+1)$, and $v_n(i) - \delta v_n(i)$ lies between $v_n(i)$ and $v_n(i-1)$.

However, with a little bit of algebra and vector calculus, one can express χ in a fashion that allows one to examine its limiting properties, namely across parallel

$(\hat{B} \parallel \vec{v})$ and perpendicular $(\hat{B} \perp \vec{v})$ shocks, where the frame in which the shock is examined is the frame in which $v_\perp$ (perpendicular component to the shock normal) is zero. From the vector identity:

$$\nabla(\vec{v} \cdot \hat{B}) = (\vec{v} \cdot \nabla)\hat{B} + (\hat{B} \cdot \nabla)\vec{v} + \vec{v} \times (\nabla \times \hat{B}) + \hat{B} \times (\nabla \times \vec{v}) \qquad \text{(A.2)}$$

one may write:

$$\chi = \hat{B} \cdot (\hat{B} \cdot \nabla)\vec{v} = \hat{B} \cdot \nabla(\vec{v} \cdot \hat{B}) - \hat{B} \cdot (\vec{v} \cdot \nabla)\hat{B} - \hat{B} \cdot [\, \vec{v} \times (\nabla \times \hat{B})\,]\,, \qquad \text{(A.3)}$$

since $\hat{B} \perp \hat{B} \times (\nabla \times \vec{v})$. In Cartesian coordinates, $\hat{B} \cdot (\vec{v} \cdot \nabla)\hat{B} = 1/2\ (\vec{v} \cdot \nabla)\hat{B}^2 = 0$ since $\hat{B}^2 = 1$, and therefore:

$$\chi = \hat{B} \cdot \nabla(\hat{B} \cdot \vec{v}) + \vec{v} \cdot [\, \hat{B} \times (\nabla \times \hat{B})\,]\,, \qquad \text{(A.4)}$$

having used the vector identity $\vec{v} \cdot [\, \hat{B} \times (\nabla \times \hat{B})\,] = -\hat{B} \cdot [\, \vec{v} \times (\nabla \times \hat{B})\,]$.

For a parallel shock $(\hat{B} = \hat{v})$ equation (A.4) reduces to

$$\chi_\parallel = \hat{v} \cdot \nabla v = \nabla \cdot (v\hat{v}) - v\nabla \cdot \hat{v} = \nabla \cdot \vec{v} \qquad \text{(A.5)}$$

for $\hat{v} = $ constant. Thus the pre to post-shock magnetic field ratio [see equation (2.14)] is $B^2/B'^2 = 1$, indicating, as expected, that the magnetic field is not affected by the shock (Fig. A.1, left).

In contrast, for a perpendicular shock ($\hat{B} \cdot \vec{v} = 0$) equation (A.4) reduces to

$$\chi_\perp = \vec{v} \cdot [\, \hat{B} \times (\nabla \times \hat{B}) \,] = 0 \tag{A.6}$$

for $\hat{B} = $ constant. From equation (2.12) it is evident that:

$$\frac{1}{B} \frac{dB}{dt} = \chi - \nabla \cdot \vec{v} \tag{A.7}$$

and therefore $dB = -B\, \nabla \cdot \vec{v}\, dt$, the same form as equation (2.7) describing the density, indicating that B scales with the density. This is the classical result of the magnetic field compression across a shock mirroring that of the density when the field is perpendicular to the shock normal (Fig. A.1, right).

In general, the magnetic field will be neither parallel nor perpendicular to the shock normal and it is expected that $0 \leq |\chi| \leq |\nabla \cdot \vec{v}|$.
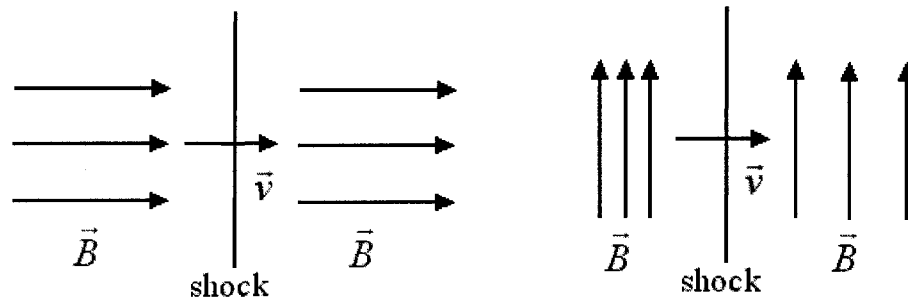

Figure A.1: Two limiting field configurations for χ: when $\vec{B} \parallel \vec{v}$ (left) $\rightarrow \chi = \nabla \cdot \vec{v}$ and the field suffers no compression at all. When $\vec{B} \perp \vec{v}$ (right) $\rightarrow \chi = 0$ and the magnetic field is maximally compressed.

Bibliography

Bagchi, J., Gopal-Krishna, Krause, M., Joshi, S., 2007, ApJ, 670, L85.

Baschek, B., 2001, The New Cosmos, Springer.

Blandford, R.D., Payne, D.G., 1982, MNRAS, 199,883.

Blundell, K.M., Rawlings, S., 2000, ApJ, 119, 1111.

Burbidge, G.R., 1956, ApJ, 124, 416.

Carilli, C.L., Barthel, P.D., 1996, A&AR, 7, 1.

Carilli, C.L., Perly, R.A., Dreher, J.W., 1988, ApJ, 334, L73.

Carilli, C.L., Perley, R.A., Dreher, J.W., Leahy, J.P., 1991, ApJ, 383, 554.

Clarke, D.A., 1996, ApJ, 457, 291.

Clarke, D.A., Burns, J.O., Norman, M.L., Loken, C., 1993, ApJ, 417, 515.

Clarke, D.A., Bridle, A.H., Burns, J.O., Perley, R.A., Norman, M.L., 1992, ApJ, 385, 173.

Clarke, D.A., Norman, M.L., Burns, J.O., 1989, ApJ, 342, 700.

Dal Pino, Elisabete M. de Gouveia, 2005, ASR, 35, 908.

Fanaroff, B.L., Riley, J.M., 1974, MNRAS, 167, 31.

Gizani, N.A.B., Leahy, J.P., 2003, MNRAS, 342, 399.

Jaffe, W.J., Perola, G.C., 1974, A&A, 26, 243.

Jester, S., Roser, H.J., Meisenheimer, K., Perley, R., Conway., 2001, A&A, 373,

447.

Jennison, R.C., Das Gupta, M.K., 1953, Nature, 172, 996.

Jones, T.W., Ryu, D., Engel, A., 1999, ApJ, 512, 105.

Kang, H., Jones, T.W., 1991, MNRAS, 249,439.

Kang, H., Jones, T.W., 1995, ApJ, 447, 944.

Kang, H., Jones, T.W., 1997, ApJ, 476, 875.

Kardashev, N.S., 1962, Soviet Astron., 6, 317.

Katz-Stone, D.M., Rudnick, L., Anderson, M.C., 1993, ApJ, 407, 549.

Katz-Stone, D.M., Rudnick, L., 1994, ApJ, 426, 116.

Katz-Stone, D.M., Rudnick, L., 1997, ApJ, 488, 146.

Katz-Stone, D.M., Rudnick, L., 1997, ApJ, 479, 258.

Katz-Stone, D.M., Rudnick, L., Butenhoff, C., Odonoghue, A.A., 1999, ApJ, 516, 716.

Koide, S., Meier, D.L., Shibata, K., Takahiro, K., 2000, ApJ, 536, 668.

Longair, M., 1994, High Energy Astrophysics, Cambridge U. Press.

Matthews, A.P., Scheuer, P.A.G., 1990, MNRAS, 242, 616.

Matthews, A.P., Scheuer, P.A.G., 1990, MNRAS, 242, 623.

Massaglia, S., 2003, astro-ph/0301148.

Massaglia, S., Bodo, G., Ferrari, A., Rossi, P., 1995, Jets from Stars and Galactic Nuclei, Springer.

Miley, G., 1980, ARAA, 18,165.

Pacholczyk, A., 1970, Radio Astrophysics, W.H. Freeman and Company.

Rudnick, L., Katz-Stone, D.M., 1996, Cygnus A-A Study of a Radio Galaxy,

Cambridge U. Press.

Rudnick, L., Katz-Stone, D.M., Anderson, M.C., 1994, ApJSS, 90, 955.

Scheuer, P.A.G., 1995, MNRAS, 277, 331.

Scheck, L., Aloy, M.A., Marti, J.M., Gomez, J.L., Muller, E., 2002, MNRAS, 331, 615.

Scheuer, P.A.G., Williams, P.J.S., 1968, ARAA, 6, 321.

Skilling,J., 1975, MNRAS, 172, 557.

Sohn, B.W., Klein, U., Mack, K.H., 2003, A&A, 404, 133.

Tregillis, I.L., Jones, T.W., Ryu, D., 2004, ApJ, 601, 778.

Tregillis, I.L., Jones, T.W., Ryu, D., 2001, ApJ, 557, 475.

Treichel, K., Rudnick, L., Hardcastle, M.J., Leahy, J.P., 2001, ApJ, 561, 691.

Weiss, N.O., 1983, GApFD, 23, 344.

Young, A., Rudnick, L., Katz, D., DeLaney, T., Kassim, N.E., Makishima, K., 2005, ApJ, 626, 748.